

A revised density split statistic model for general filters

Pierre Burger¹, Oliver Friedrich^{2,3}, Joachim Harnois-Déraps^{4,5}, and Peter Schneider¹

¹ Argelander-Institut für Astronomie, Auf dem Hügel 71, 53121 Bonn, Germany

² Kavli Institute for Cosmology, University of Cambridge, CB3 0HA Cambridge, UK

³ Churchill College, University of Cambridge, CB3 0DS Cambridge, UK

⁴ School of Mathematics, Statistics and Physics, Newcastle University, Newcastle upon Tyne, NE1 7RU, UK

⁵ Astrophysics Research Institute, Liverpool John Moores University, 146 Brownlow Hill, Liverpool L3 5RF, UK
e-mail: pburger@astro.uni-bonn.de

Received XXX; accepted XXX

ABSTRACT

Context. Studying the statistical properties of the large-scale structure in the Universe with weak gravitational lensing is a prime goal of several current and forthcoming galaxy surveys. The power that weak lensing has to constrain cosmological parameters can be enhanced by considering statistics beyond second-order shear correlation functions or power spectra. One such higher-order probe that has proven successful in observational data is the density split statistics (DSS), in which one analyses the mean shear profiles around points that are classified according to their foreground galaxy density.

Aims. In this paper, we generalise the most accurate DSS model (Friedrich et al. 2018) to allow for a broad class of angular filter functions used for the classification of the different local density regions. This approach is motivated by earlier findings showing that an optimised filter can provide tighter constraints on model parameters compared to the standard top-hat case.

Methods. As in the previous DSS model we build on large deviation theory approaches and approximations thereof to model the matter density PDF, and on perturbative calculations of higher-order moments of the density field. The novel addition relies on the generalisation of these previously employed calculations to allow for general filter functions and is validated on several sets of numerical simulations.

Results. It is shown that the revised model fits well the simulation measurements for many filter choices, with a residual systematic offset that is small compared to the statistical accuracy of current weak lensing surveys. We find that the accuracy of the model is slightly lower for a compensated filter than for a non-negative filter function, and that it increases with the filter size. Using a Fisher matrix approach, we study the expected sensitivity of the DSS to cosmological parameters, exploring different data compression strategies, and find constraints comparable to the commonly used two-point cosmic shear measures. Hence, our DSS model can be used in competitive analyses of current cosmic shear data, while it may need refinements for forthcoming lensing surveys.

Key words. gravitational lensing: weak – methods: statistical – surveys – Galaxy: abundances – (cosmology:) large-scale structure of Universe

1. Introduction

Studying the matter distribution of the present large-scale structure reveals a wealth of information about the evolution of the Universe. In particular, its distorting effect on the propagation of light from distant galaxies, dubbed *cosmic shear*, can be captured by analysing weak lensing surveys. By comparing the results of cosmological models with the observed signal, one can constrain cosmological parameters (see e.g. Asgari et al. 2021; DES Collaboration et al. 2021; Hamana et al. 2020).

The preferred methods to infer statistical properties of the matter and galaxy distribution concentrate on the second-order statistics, like the two-point correlation functions or their Fourier counterparts, the power spectra. Although these statistics have an impressive accuracy to describe for instance primordial perturbations visible in the cosmic microwave background (CMB; e.g. Planck Collaboration et al. 2020) they probe only the Gaussian information present in the density fluctuations. However, these initial conditions developed significant non-Gaussian features by means of non-linear gravitational instability, which can only be investigated with higher-order statistics. Although these are typically more time consuming to model and measure, these higher-order statistics scale differently with cosmological pa-

rameters, and are not affected in the same way by residual systematics. Hence, by jointly investigating second- and higher-order statistics, the constraining power on cosmological parameters increases (see, e.g. Bergé et al. 2010; Pyne & Joachimi 2021; Pires et al. 2012; Fu et al. 2014; Kilbinger & Schneider 2005).

Whereas in the literature a large number of analytical models for the two-point statistics exists (Takahashi et al. 2012; Heitmann et al. 2014; Euclid Collaboration et al. 2020; Mead et al. 2020; Nishimichi et al. 2021), the analysis of higher-order statistics are usually based on simulations. Analytical models for higher-order lensing statistics are rare, although they are important not only for scientists to understand physical processes but also to cross check simulations, which are usually only tested against Gaussian statistics. For example, Reimberg & Bernardeau (2018) and Barthelemy et al. (2021) used large deviation theory (LDT) to compute the reduced-shear correction to the aperture mass probability distribution function (PDF); Munshi et al. (2020) and Halder et al. (2021) modelled analytically the integrated shear three-point function; the lensing peak count function has been modelled in Fan et al. (2010); Lin & Kilbinger (2015); Shan et al. (2018), while the lensing PDF has been modelled in Boyle et al. (2020).

The examples mentioned above all concern the analysis of cosmic shear data. However, it has been established in recent analyses that the addition of foreground clustering data, and their cross-correlation with the background source galaxies, yield significantly better constraints (Abbott et al. 2018; Heymans et al. 2021). While the central analyses focused again on two-point statistics, Friedrich et al. (2018, hereafter F18) developed a competitive model based on the so-called *density split statistics* (hereafter DSS). The idea is to measure the mean tangential shear around small sub-areas of the survey, and to stack the signal according to the foreground galaxy density in these sub-areas. One expects the tangential shear to be larger around points with a high density of foreground galaxies, given that these correspond to a large matter over-density on average. The model derived in F18 is based on non-perturbative calculations of the matter density PDF, which predicts the shear profiles and the probability density of galaxy counts in the sub-areas, for a given cosmological model, a redshift distribution for the source and lens galaxy populations, and a mean galaxy density. In Gruen et al. (2018, hereafter G18), the F18 model is used to constrain cosmological parameters from DSS measurements from the Dark Energy Survey (DES) First Year and Sloan Digital Sky Survey (SDSS) data, which yields constraints on the matter density $\Omega_m = 0.26^{+0.04}_{-0.03}$ that agree and are competitive with the DES analysis of galaxy and shear two-point functions (see Abbott et al. 2018).

The prime motivation for this work is based on Burger et al. (2020, hereafter B20), where it is shown with a suite of numerical simulations that using matched filter functions for searching peaks and troughs in the galaxy and matter density contrast has clear advantages compared to the top-hat filter used in the F18 model, both in terms of the overall signal S/N and in recovering accurately the galaxy bias term. Smoothing cosmic density fields with filters other than top-hat ones significantly complicates the LDT-like calculations used by F18 and G18 (cf. Barthelemy et al. 2021). This is because for top-hat filters the Lagrangian to Eulerian mapping inherent in LDT is particularly simple. However, we find here that density split statistics with non-top-hat filters that are sufficiently concentrated around their centres can still be accurately modelled with computationally feasible extensions of approximations made by F18. This paper describes our modifications to the F18 model, which will allow us to optimise filtering strategies when applying density split statistics to Stage-III weak lensing surveys such as KiDS. Throughout this paper, if not otherwise stated we assume a spatially flat universe.

This work is structured as follows. In Sect. 2 we review the basics of the aperture statistics, then detail our changes to the F18 model in Sect. 3. In Sect. 4 we describe the simulations as well as the construction of our mock data, that are used to validate the revised model. In Sect. 5 we compare the model predictions with simulations, and establish its limitations. We summarise our work in Sect. 6.

2. Aperture statistics

The lensing convergence κ and shear γ are related via the lensing potential ψ (Schneider et al. 1992) as

$$\kappa(\theta) = \frac{1}{2}(\partial_1^2 + \partial_2^2)\psi(\theta), \quad \gamma(\theta) = \frac{1}{2}(\partial_1^2 - \partial_2^2 + 2i\partial_1\partial_2)\psi(\theta), \quad (1)$$

with $\partial_i = \frac{\partial}{\partial\theta_i}$, θ is the angular position on the sky and we have employed the flat-sky approximation. Given a reference point in a Cartesian coordinate system on the sky and a second point

whose separation to the first is oriented at an angle ϕ with respect to that coordinate system, we can express the shear at the second point in terms of the tangential and cross shear with respect to the first point as

$$\gamma_t = -\text{Re}(\gamma e^{-2i\phi}), \quad \gamma_\times = -\text{Im}(\gamma e^{-2i\phi}), \quad (2)$$

where the factor 2 in the exponent is due to the polar nature of the shear. Given a convergence field $\kappa(\theta)$, the aperture mass at position θ is defined as

$$M_{\text{ap}}(\theta) := \int d^2\theta' \kappa(\theta + \theta') U(|\theta'|), \quad (3)$$

where $U(\vartheta)$ is a compensated, axisymmetric filter function, such that $\int \vartheta U(\vartheta) d\vartheta = 0$. As shown in Schneider (1996), if U is compensated, M_{ap} can also be expressed in terms of the tangential shear γ_t and a related filter function Q as

$$M_{\text{ap}}(\theta) = \int d^2\theta' \gamma_t(\theta + \theta') Q(|\theta'|), \quad (4)$$

where

$$Q(\vartheta) = \frac{2}{\vartheta^2} \int_0^\vartheta d\vartheta' \vartheta' U(\vartheta') - U(\vartheta), \quad (5)$$

which can be inverted, yielding

$$U(\vartheta) = 2 \int_\vartheta^\infty d\vartheta' \frac{Q(\vartheta')}{\vartheta'} - Q(\vartheta). \quad (6)$$

In analogy to M_{ap} , we define, as done in B20, the aperture number counts (Schneider 1998), or aperture number, as

$$N_{\text{ap}}(\theta) := \int d^2\theta' n(\theta + \theta') U(|\theta'|), \quad (7)$$

where $U(\vartheta)$ is the same filter function as in Eq. (3) and $n(\vartheta)$ is the (foreground) galaxy number density on the sky. This definition of the aperture number is equivalent to the ‘Counts-in-Cell’ (CiC) from Gruen et al. (2016) if one uses a top-hat filter of the form

$$U_{\text{th}}(\vartheta) = \frac{1}{A} \mathcal{H}(\vartheta_{\text{th}} - \vartheta), \quad (8)$$

where \mathcal{H} is the Heaviside step function and A is the area of the filter. However, B20 demonstrated that top-hat filters are not optimal, and that a better performance is achieved by an adapted filter in terms of signal-to-noise-ratio (S/N) and in recovering accurately the galaxy bias term. In this paper, we compute aperture mass statistics with Eq. (4) using simulated weak lensing catalogues of background source galaxies, notably regarding positions and ellipticities, and aperture number statistics with Eq. (7) from the position of simulated foreground lens galaxies (see Sect. 4).

3. Revised model

In this section we describe our modifications of the original F18 model. Although the derivations shown here are self-contained, we recommend the interested reader to consult the original F18 paper. Especially, it is shown there that the full non-perturbative calculation of the probability density function (PDF) within

large deviation theory (LDT) can well be approximated with a log-normal PDF that matches variance and skewness of the LDT result. This allowed F18 and G18 to replace the expensive LDT computation with a faster one, hence making the calculation of full Monte-Carlo-Markov chains feasible. The reason why this approximation works well is that – for top-hat filters – the scaling of variance and higher-order cumulants in LDT is similar to that found in log-normal distributions. This cannot a priori be expected for other filter functions. However, through comparison with N-body simulations we find here (cf. Sect. 5) that either a simple log-normal or a combination of two log-normal distributions still accurately describes the density PDFs required to analyse density split statistics with more general classes of filters. The following section describes these calculations. In order to reduce the mathematical calculations in this section, some derivations are detailed in Appendix A.

We start by defining the line-of-sight projection of the 3D matter density contrast $\delta_{m,3D}$, weighted by a foreground (lens) galaxy redshift probability distribution $n_f(z)$ as

$$\delta_{m,2D}(\theta) = \int d\chi q_f(\chi) \delta_{m,3D}(\chi\theta, \chi), \quad (9)$$

where χ is the co-moving distance and the projection kernel $q_f(\chi)$ is

$$q_f(\chi) = n_f(z[\chi]) \frac{dz[\chi]}{d\chi}. \quad (10)$$

This 2D matter density contrast can then be used together with a linear bias term to represent a tracer density contrast (see Sect. 3.3 or Sect. 4). Following F18, the next step consists of smoothing the results with a filter U of size Θ :

$$\delta_{m,U}(\theta) = \int_{|\theta'| < \Theta} d^2\theta' \delta_{m,2D}(\theta + \theta') U(|\theta'|), \quad (11)$$

which simplifies in case of a top-hat filter of size Θ to

$$\delta_{m,th}^\Theta(\theta) = \frac{1}{A} \int_{|\theta'| < \Theta} d^2\theta' \delta_{m,2D}(\theta + \theta'). \quad (12)$$

Similar to the 2D density contrast, the convergence, which is needed to describe the DSS signal, is given by

$$\kappa(\theta) = \int d\chi W_s(\chi) \delta_{m,3D}(\chi\theta, \chi), \quad (13)$$

where $W_s(\chi)$ is the lensing efficiency defined as

$$W_s(\chi) = \frac{3\Omega_m H_0^2}{2c^2} \int_{\chi'}^\infty d\chi' \frac{\chi(\chi' - \chi)}{\chi' a(\chi)} q_s(\chi'), \quad (14)$$

with $q_s(\chi) = n_s(z[\chi]) \frac{dz[\chi]}{d\chi}$ being the line-of-sight probability density of the sources, Ω_m the matter density parameter, H_0 the Hubble parameter and c the speed-of-light. The mean convergence inside an angular separation θ , $\kappa_{<\theta}$, follows then in analogy to Eq. (12) by substituting $\delta_{m,2D}(\theta)$ with $\kappa(\theta)$.

The aim of our model is to predict the tangential shear profiles γ_t given a quantile Q of the foreground aperture number N_{ap} , $\langle \gamma_t | Q \rangle$, where for instance the highest quantile is the set of line-of-sights of the sky that have the highest values of N_{ap} . Therefore, to determine $\langle \gamma_t | Q \rangle$ the model calculates $\langle \gamma_t | N_{ap} \rangle$ and sums

up all that belong to the corresponding quantile Q . The expectation value of $\langle \gamma_t | N_{ap} \rangle$ is computed from the convergence profile as

$$\langle \gamma_t(\theta) | N_{ap} \rangle = \langle \kappa_{<\theta} | N_{ap} \rangle - \langle \kappa_\theta | N_{ap} \rangle = -\frac{\theta}{2} \frac{d}{d\theta} \langle \kappa_{<\theta} | N_{ap} \rangle, \quad (15)$$

where κ_θ is the azimuthally averaged convergence at angular separation θ from the centre of the filter, and $\kappa_{<\theta}$ is the average convergence inside that radius. The latter quantity, conditioned on a given N_{ap} , can be specified by

$$\langle \kappa_{<\theta} | N_{ap} \rangle = \int d\delta_{m,U} \langle \kappa_{<\theta} | \delta_{m,U}, N_{ap} \rangle p(\delta_{m,U} | N_{ap}) \quad (16)$$

$$\approx \int d\delta_{m,U} \langle \kappa_{<\theta} | \delta_{m,U} \rangle p(\delta_{m,U} | N_{ap}), \quad (17)$$

where in the second step we assumed that the expected convergence within θ only depends on the projected matter density contrast $\delta_{m,U}$ and not on the particular realisation of shot-noise in N_{ap} found within that fixed matter density contrast¹.

By use of Bayes' theorem, we can express the conditional PDF as

$$p(\delta_{m,U} | N_{ap}) = \frac{p(N_{ap} | \delta_{m,U}) p(\delta_{m,U})}{p(N_{ap})}, \quad (18)$$

where $p(N_{ap} | \delta_{m,U})$ is the probability of finding N_{ap} given the smoothed density contrast $\delta_{m,U}$. The normalisation in the denominator of Eq. (18) follows by integrating over the numerator,

$$p(N_{ap}) = \int d\delta_{m,U} p(\delta_{m,U}) p(N_{ap} | \delta_{m,U}). \quad (19)$$

As seen in the derivation above, we are left with three ingredients in order to calculate the tangential shear profiles given a quantile Q of the aperture number $\langle \gamma_t(\theta) | N_{ap} \rangle$:

- (I) The PDF of the matter density contrast smoothed with the filter function U (used in Eqs. 18, 19)

$$p(\delta_{m,U}). \quad (20)$$

- (II) The expectation value of the convergence inside a radius θ given the smoothed density contrast (used in Eq. 17)

$$\langle \kappa_{<\theta} | \delta_{m,U} \rangle. \quad (21)$$

- (III) The distribution of N_{ap} for the given filter function U given the smoothed density contrast (used in Eqs. 18, 19)

$$p(N_{ap} | \delta_{m,U}). \quad (22)$$

Since all three ingredients are sensitive to the filter U we need to adjust all of them coherently with respect to the top-hat case.

¹ This assumption is not per se evident, since via mode coupling the large-scale profile of a given density perturbation may well be correlated to the shot-noise (i.e., small-scale fluctuations) of galaxy formation in the centre of that perturbation. F18 have found the approximation $\langle \kappa_{<\theta} | \delta_{m,U}, N_{ap} \rangle \approx \langle \kappa_{<\theta} | \delta_{m,U} \rangle$ to be accurate in the Buzzard N-body simulations (DeRose et al. 2019) but a more stringent investigation of this assumption is left for future work.

3.1. (I) : $p(\delta_{m,U})$

F18 have shown that one can accurately approximate the full LDT computation of the matter density PDF by a shifted log-normal distribution with vanishing mean (Hilbert et al. 2011), which is fully characterised by two parameters, σ and δ_0 , as

$$p(\delta_{m,U}) = \frac{1}{\sqrt{2\pi}\sigma(\delta_{m,U} + \delta_0)} \exp\left(-\frac{[\ln(\delta_{m,U}/\delta_0 + 1) + \sigma^2/2]^2}{2\sigma^2}\right). \quad (23)$$

The two free parameters can be determined by specifying the variance $\langle\delta_{m,U}^2\rangle$ and skewness $\langle\delta_{m,U}^3\rangle$ of the PDF as (Hilbert et al. 2011)

$$\langle\delta_{m,U}^2\rangle = \delta_0^2 [\exp(\sigma^2) - 1], \quad (24)$$

$$\langle\delta_{m,U}^3\rangle = \frac{3}{\delta_0} \langle\delta_{m,U}^2\rangle^2 + \frac{1}{\delta_0^3} \langle\delta_{m,U}^2\rangle^3, \quad (25)$$

where we derive the expression of $\langle\delta_{m,U}^2\rangle$ and $\langle\delta_{m,U}^3\rangle$ in Appendix A (see Eq. A.28).

As we will see later, this approximation works well for non-negative filter functions like top-hat or Gaussian filters. However, the log-normal PDF approximation becomes less accurate for compensated filters that include negative weights. In these cases, we instead divide U into $U_>(\vartheta) = U(\vartheta)\mathcal{H}(\vartheta_{\text{ts}} - \vartheta)$ and $U_<(\vartheta) = -U(\vartheta)\mathcal{H}(\vartheta - \vartheta_{\text{ts}})$, where ϑ_{ts} is the transition scale from positive to negative filter weights. As a consequence, we obtain two correlated log-normal random variables, $\delta_{m,U_>}$ and $\delta_{m,U_<}$, whose joint distribution can be represented by a bi-variate log-normal distribution as

$$p(\delta_{m,U_>}, \delta_{m,U_<}) = \frac{1}{2\pi\sigma_>(\delta_{m,U_>} + \delta_{0,>})\sigma_<(\delta_{m,U_<} + \delta_{0,<})\sqrt{1-\rho^2}} \times \exp\left(-\frac{1}{2(1-\rho^2)} [\Delta_>^2 + \Delta_<^2 - 2\rho\Delta_>\Delta_<]\right), \quad (26)$$

where we defined

$$\Delta_> = \frac{\ln(\delta_{m,U_>}/\delta_{0,>} + 1) + \sigma_>^2/2}{\sigma_>}, \quad (27)$$

and similarly for $\Delta_<$. The correlation coefficient ρ is determined by

$$\rho = \ln\left(\frac{\langle\delta_{m,U_>}\delta_{m,U_<}\rangle}{\delta_{0,>}\delta_{0,<}} + 1\right) \frac{1}{\sigma_>\sigma_<}, \quad (28)$$

and in order to calculate the difference of two independent random variables $\delta_{m,U} = \delta_{m,U_>} - \delta_{m,U_<}$ we can use the convolution theorem² to get

$$p(\delta_{m,U}) = \int_{-\infty}^{\infty} d\delta_{m,U_>} p(\delta_{m,U_>}, \delta_{m,U_>} - \delta_{m,U}). \quad (29)$$

² <http://statweb.stanford.edu/~susan/courses/s116/node114.html>

3.2. (II) : $\langle\kappa_{<\vartheta}|\delta_{m,U}\rangle$

In order to calculate the expectation value of the mean convergence inside an angular radius ϑ , $\kappa_{<\vartheta}$, given the matter density contrast $\delta_{m,U}$, we assume that both follow a joint log-normal distribution (see e.g. the discussion in Appendix B of G18). In this case, the expectation value can be written as

$$\frac{\langle\kappa_{<\vartheta}|\delta_{m,U}\rangle}{\kappa_0} = \exp\left(\frac{C [2 \ln(\delta_{m,U}/\delta_0 + 1) + V - C]}{2V}\right) - 1, \quad (30)$$

where δ_0 is determined with Eq. (25) and the three variables C , V , and κ_0 can be calculated from the moments $\langle\delta_{m,U}^2\rangle$, $\langle\kappa_{<\vartheta}|\delta_{m,U}\rangle$ and $\langle\kappa_{<\vartheta}|\delta_{m,U}^2\rangle$, which follow from the derivation in Appendix A (see Eq. A.29),

$$V = \ln\left(1 + \frac{\langle\delta_{m,U}^2\rangle}{\delta_0^2}\right), \quad (31)$$

$$C = \ln\left(1 + \frac{\langle\kappa_{<\vartheta}|\delta_{m,U}\rangle}{\delta_0\kappa_0}\right), \quad (32)$$

$$\kappa_0 = \frac{\langle\kappa_{<\vartheta}|\delta_{m,U}\rangle^2 e^V}{\langle\kappa_{<\vartheta}|\delta_{m,U}^2\rangle - 2\langle\kappa_{<\vartheta}|\delta_{m,U}\rangle\langle\delta_{m,U}^2\rangle/\delta_0}. \quad (33)$$

We note that the assumption that $\delta_{m,U}$ is log-normal distributed is not well justified for filters with negative weights as we mentioned in the previous section. A possible improvement could be done for instance by assuming again that $\delta_{m,U}$ is made up of two log-normal random variables, such that we would need to calculate conditional moments like $\langle\kappa_{<\vartheta}|\delta_{m,U_>} - \delta_{m,U_<}\rangle$. This would significantly increase the amount of joint moments needed in our calculation and would render fast modelling unfeasible. However, such an improved modelling is also unnecessary at present, given the statistical uncertainties we expect for Stage-III weak lensing surveys such as KiDS-1000. We demonstrate this empirically in Sect. 5 by comparison to N-body simulated data. But we also want to give a brief theoretical motivation: The average value of $\kappa_{<\vartheta}$ given that $\delta_{m,U}$ lies within the range $[\delta_{\min}, \delta_{\max}]$ is given by

$$\langle\kappa_{<\vartheta}|\delta_{m,U} \in [\delta_{\min}, \delta_{\max}]\rangle = \frac{\int_{\delta_{\min}}^{\delta_{\max}} d\delta_{m,U} p(\delta_{m,U}) \langle\kappa_{<\vartheta}|\delta_{m,U}\rangle}{\int_{\delta_{\min}}^{\delta_{\max}} d\delta_{m,U} p(\delta_{m,U})}. \quad (34)$$

If $\kappa_{<\vartheta}$ and $\delta_{m,U}$ were joint Gaussian random variables, then $p(\delta_{m,U})$ would be a Gaussian PDF and we would have $\langle\kappa_{<\vartheta}|\delta_{m,U}\rangle = \delta_{m,U} \langle\delta_{m,U}\kappa_{<\vartheta}\rangle/\langle\delta_{m,U}^2\rangle$. We now argue that the leading-order correction to this Gaussian approximation consists of replacing $p(\delta_{m,U})$ by our full non-Gaussian model, without changing $\langle\kappa_{<\vartheta}|\delta_{m,U}\rangle$, since this would be exactly correct in the limit of strong correlation between the two variables. Our log-normal approximation to $\langle\kappa_{<\vartheta}|\delta_{m,U}\rangle$ is then already a next-to-leading-order correction and a bi-variate log-normal approximation for $\langle\kappa_{<\vartheta}|\delta_{m,U}\rangle$ would be of even higher order. While this reasoning is admittedly only heuristic, it is proven correct by the accuracy of our model predictions for the lensing signals in Sect. 5 (cf. Fig. 6).

3.3. (III) : $p(N_{\text{ap}}|\delta_{m,U})$

The third basic ingredient is the PDF of N_{ap} given the projected matter density contrast smoothed with the filter U . Assuming a Poisson distribution for N_{ap} , which is the most straightforward ansatz, is unfortunately not possible due the fact that negative

values are expected with a compensated filter (i.e. in some of the $U_{<}$ contribution). We use instead a completely new approach compared to F18, and derive an expression for $p(N_{\text{ap}}|\delta_{\text{m},U})$ by use of the ‘characteristic function’ (Papoulis & Pillai 1991, hereafter CF), which is an alternative representation of a probability distribution, similar to the moment generating functions, but based on the Fourier transform of the PDF. Of interest to us, the n -th derivative of the CFs can be used to calculate the n -th moment of the PDF. The CF corresponding to $p(N_{\text{ap}}|\delta_{\text{m},U})$ is defined as

$$\Psi(t) = \langle e^{itN_{\text{ap}}} \rangle_{\delta_{\text{m},U}} = \int_{\mathbb{R}} dN_{\text{ap}} p(N_{\text{ap}}|\delta_{\text{m},U}) e^{itN_{\text{ap}}}, \quad (35)$$

where in our particular case, we derive in Appendix A.4 a closed expression as

$$\Psi(t) = \exp \left(2\pi n_0 \int_0^\infty d\vartheta \vartheta (1 + b \langle w_\vartheta | \delta_{\text{m},U} \rangle) [e^{itU(\vartheta)} - 1] \right) \quad (36)$$

with n_0 being the mean number density of foreground galaxies on the sky. The assumption of linear galaxy bias enters here by the term $b \langle w_\vartheta | \delta_{\text{m},U} \rangle$, with

$$w_\vartheta = \frac{1}{2\pi} \int_0^{2\pi} d\phi \delta_{\text{m},2D}(\vartheta, \phi). \quad (37)$$

Hence, $n_0(1 + b \langle w_\vartheta | \delta_{\text{m},U} \rangle)$ is the effective number density at ϑ given $\delta_{\text{m},U}$. The conditional expectation value $\langle w_\vartheta | \delta_{\text{m},U} \rangle$ is given in analogy to Eq. (30), but with replacing $\langle \kappa_{<\vartheta} \delta_{\text{m},U}^k \rangle \rightarrow \langle w_{<\vartheta} \delta_{\text{m},U}^k \rangle$ in Eqs. (31–33) for $k = 1, 2$ and using that

$$\langle w_\vartheta | \delta_{\text{m},U} \rangle = \langle w_{<\vartheta} | \delta_{\text{m},U} \rangle + \frac{\vartheta}{2} \frac{d}{d\vartheta} \langle w_{<\vartheta} | \delta_{\text{m},U} \rangle, \quad (38)$$

where the joint moments $\langle w_{<\vartheta} \delta_{\text{m},U}^k \rangle$ are also derived in Appendix A (see Eq. A.30). Next, we re-express Eq. (36) as the product of two terms,

$$\Psi(t) = \exp[p(t)] \exp[iq(t)], \quad (39)$$

where

$$p(t) = 2\pi n_0 \int_0^{R_{\text{max}}} d\vartheta \vartheta (1 + b \langle w_\vartheta | \delta_{\text{m},U} \rangle) (\cos[tU(\vartheta)] - 1), \quad (40)$$

$$q(t) = 2\pi n_0 \int_0^{R_{\text{max}}} d\vartheta \vartheta (1 + b \langle w_\vartheta | \delta_{\text{m},U} \rangle) \sin[tU(\vartheta)], \quad (41)$$

and R_{max} is the angular radius beyond which U vanishes. We note that G18 and F18 found super-Poisson shot-noise in their work. They interpret these deviations from Poisson noise as having a number $\neq 1$ of galaxies per ‘Poisson halo’. This would suggest that we could incorporate non-Poissonian behaviour by replacing n_0 with an effective density of Poisson halos and making this a free parameter of our model. However, more recent investigations (e.g. Friedrich et al. in prep.) cast doubt on the simplified interpretation of F18 and G18. A proper investigation of the problem of non-Poissonian shot-noise is beyond the scope of this work, and we will address it in future investigations.

Finally, the probability density function $p(N_{\text{ap}}|\delta_{\text{m},U})$ follows from the inverse Fourier transform of the CF

$$\begin{aligned} p(N_{\text{ap}}|\delta_{\text{m},U}) &= \frac{1}{2\pi} \int_{\mathbb{R}} dt \exp(-itN_{\text{ap}}) \Psi(t) \\ &= \frac{1}{2\pi} \int_{\mathbb{R}} dt \cos(q(t) - tN_{\text{ap}}) \exp[p(t)], \end{aligned} \quad (42)$$

where the second step follows from the fact that the imaginary part cancels.

In Appendix A.4 we discuss a similar approach, where we assume that $p(N_{\text{ap}}|\delta_{\text{m},U})$ is log-normal distributed. In that case, to specify the PDF, only the first three moments are needed, which follow from derivatives of the CF. As shown in Appendix A.4 both methods yield almost identical results, and since the log-normal approach is significantly faster, we opted for it hereafter, unless otherwise stated.

4. Simulation data

Before using our revised model in data analyses, it is mandatory to quantify its precision and range of validity. We use for this validation exercise three simulations suites:

- the full-sky gravitational lensing simulations described in Takahashi et al. (2017, T17 hereafter), with which we carry out a detailed investigation of the model in a simple survey configuration,
- the cosmo-SLICS simulations, described in Harnois-Déraps et al. (2019), with which we explore the cosmology dependence in a KiDS-1000-like survey,
- the SLICS simulations (Harnois-Déraps et al. 2018), from which we estimate the lensing covariance matrix in this survey configuration.

4.1. T17 simulations

The T17 simulations are constructed from a series of nested cubic boxes with side lengths of $L, 2L, 3L, \dots$ placed around a fixed vertex representing the observer’s position, with $L = 450 \text{ Mpc}/h$. Each box is replicated eight times and placed around the observer using periodic boundary conditions. The number of particles per box is fixed to 2048^3 , which results in higher mass and spatial resolutions at lower redshifts. Within each box, three spherical lens shells are constructed, each with a width of $150 \text{ Mpc}/h$, which are then used by the public code GRAYTRIX³ to trace the light-ray trajectories from the observer to the last scattering surface⁴. With the N -body code GADGET2 (Springel et al. 2001) the gravitational evolution of dark matter particles without baryonic processes are followed from the initial conditions, which in turn are determined by use of second-order Lagrangian perturbation theory. The initial linear power spectrum followed from the Code for Anisotropies in the Microwave Background (Lewis et al. 2000, CAMB) with $\Omega_{\text{m}} = 1 - \Omega_{\Lambda} = 0.279$, $\Omega_{\text{b}} = 0.046$, $h = 0.7$, $\sigma_8 = 0.82$, and $n_{\text{s}} = 0.97$. The matter power spectrum agrees with theoretical predictions of the revised Halofit (Takahashi et al. 2012) within 5%(10%) for $k < 5(6) h \text{ Mpc}^{-1}$ at $z < 1$. In order to account for the finite shell thickness and angular resolution, T17 provide correction formulae that we repeat in Appendix B. Although various resolution options are available, for our purpose the realisations with a resolution of $N_{\text{SIDE}} = 4096$ are sufficient.

We use the publicly available matter density contrast maps to create a realistic lens galaxy catalogue that mimics the second and third redshift bins of the luminous red galaxies sample constructed from the KiDS-1000 data (Vakili et al. 2019), as shown by the solid lines in Fig. 1. The reason to mock the LRG sample is that the galaxy bias for this kind of galaxies

³ <http://th.nao.ac.jp/MEMBER/hamanatk/GRAYtrix/>

⁴ These maps are freely available for download at http://cosmo.phys.hirosaki-u.ac.jp/takahasi/allsky_raytracing/

can be roughly described with a constant linear bias, which is needed for the analytical model. We excluded the lowest-redshift lens bin, first because of its low galaxy number density ($n_0 = 0.012 \text{ gal/arcmin}^2$) in which the shot noise level is significant, and second because the density field is more non-linear, and hence, we expect the log-normal approximation to break down. Since there is a significant overlap between the KiDS-1000 sources and the lenses in the fourth LRG redshift bin, we reject it as well. To create our lens galaxy samples we first project the T17 3D-density maps $\delta_{m,3D}$ following the $n(z)$ shown as the step functions in Fig. 1 to get two $\delta_{m,2D}$ maps. For both maps we then distribute galaxies following a Poisson distribution with parameter $\lambda = n(1 + b \delta_{m,2D})$, where b is a constant linear galaxy bias and n is chosen such that the galaxy number density is $n_0 = 0.028 \text{ gal/arcmin}^2$ for the second bin (hereafter low-redshift bin $z_{l,low}$) and $n_0 = 0.046 \text{ gal/arcmin}^2$ for the third lens bin (hereafter high-redshift bin $z_{l,high}$). Since our method requires a constant linear galaxy bias, we specify a bias of 1.72 for lens bin two and 1.74 for lens bin three, similar to those reported in Vakili et al. (2019). F18 found this linear bias assumption to be accurate enough for year-1 data of the Dark Energy Survey, which is similar in constraining power to our target KiDS data (but note that an investigation of higher-order biasing is underway in Friedrich et al., in prep.).

In our validation test, we use a shear grid at a single source plane located at $z = 0.8664$, indicated by the black dashed line in Fig. 1. F18 showed already that the model works for realistic redshift distributions, and this choice simplifies the generation of our source catalogues. Furthermore, in order to determine a realistic covariance matrix, we transform the shear field into an observed ellipticity field by adding shape noise to the shear grid as

$$\epsilon^{\text{obs}} = \frac{\epsilon^s + g}{1 + \epsilon^s g^*}, \quad (43)$$

where ϵ^{obs} , ϵ^s and g are complex numbers, and the asterisk ‘*’ indicates complex conjugation. The source ellipticities ϵ^s per pixel are generated by drawing random numbers from a Gaussian distribution with width

$$\sigma_{\text{pix}} = \frac{\sigma_\epsilon}{\sqrt{n_{\text{gal}} A_{\text{pix}}}} \approx 0.29, \quad (44)$$

where A_{pix} is the pixel area of the shear grid, and the effective number density n_{gal} and σ_ϵ are chosen such that they are consistent with the KiDS data. While this transformation is valid in terms of the reduced shear $g = \gamma/(1 - \kappa)$, we will use throughout this paper the approximation $\gamma \approx g$, as the typical values for the convergence are small, $|\kappa| \ll 1$. We are neglecting the intrinsic alignment of galaxies in this work.

4.2. Extracting the model components from the T17 simulations

In order to validate the different components of our model, we need to extract $p(\delta_{m,U})$, $p(N_{\text{ap}})$ and $\langle \gamma_l | Q \rangle$ from the simulation. The first two follow directly by smoothing the maps of the projected density contrast and the lens galaxy with the corresponding filters. This smoothing can be performed in two different ways. The first is to use the HEALPY function `QUERY_DISC`, which finds all pixel centres that are located within a given radius, whereas the second approach uses the HEALPY function `SMOOTHING`, with a given beam window function created by the function `BEAM2BL`. Both approaches result in PDFs that differ

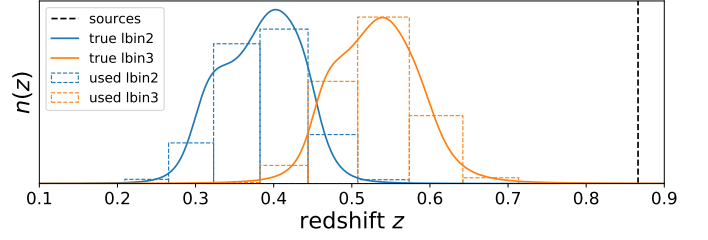


Fig. 1: Lens galaxy redshift distribution, where the solid lines are the true $n(z)$ of the second $z_{l,low}$ and third $z_{l,high}$ LRG bin (Vakili et al. 2019). The coloured dashed histograms show the redshift distribution constructed from the T17 simulation, while the black dashed line shows the redshift of the source galaxies.

slightly, since the `QUERY_DISC` does not reproduce an exact top-hat, while the `SMOOTHING` approach is only over a finite ℓ -range. Nevertheless we found that both approaches are consistent for $N_{\text{SIDE}} = 4096$ well within the uncertainty we estimate from 48 sub-patches (see discussion below), and hence use the second approach which is significantly faster.

The tangential shear information $\langle \gamma_l | Q \rangle$ is measured for each quantile Q by the software `TREECORR` (Jarvis et al. 2004) in 15 log-spaced bins with angular separation $\Theta/20 < \vartheta < \Theta$, where Θ is the size of the filter being used. For the top-hat filter we measured the shear profiles from $6' < \vartheta < 120'$, corresponding to a filter with a size of $120'$. We note here that for all measured shear profiles the shear around random points is always subtracted, which ensures that the shear averaged over all quantiles for one realisation vanishes by definition.

In order to have an uncertainty for all the three model quantities, we divide the full-sky map into 48 sub-patches, such that each patch has a size of approximately 859.4 deg^2 . For $p(\delta_{m,U})$ and $p(N_{\text{ap}})$ we determined for each sub-patch one distribution, such that we were able to calculate a standard deviation from 48 values for each bin in the PDF. For the covariance matrix we use 10 out of the 108 realizations and divide each full-sky map in 48 sub-patches, which then results in a covariance matrix measured from 480 fields. Furthermore, both for the covariance and for the error-bars in the plotted shear profiles we use Eq. (43) to create noisy shear profiles for each sub-patch, which are then re-scaled to the effective KiDS-1000 area (see Giblin et al. 2020).

4.3. Cosmo-SLICS

We use the cosmo-SLICS simulations described in Harnois-Déraps et al. (2019) to determine the validity regime of our revised model for different cosmologies. These are a suite of weak lensing simulations sampling 26 points (listed in Table C.1) in a broad w CDM parameter space, distributed in a Latin hypercube to minimise interpolation errors. Specifically, the matter density Ω_m , the dimensionless Hubble parameter h , the normalisation of the matter power spectrum σ_8 and the time-independent equation-of-state parameter of dark energy w_0 are varied over a range that is large enough to complement the analysis of current weak lensing data (see e.g. Harnois-Déraps et al. 2020). Each simulation follows 1536^3 particles inside a cube of comoving side length $L_{\text{box}} = 505 h^{-1} \text{ Mpc}$ and $n_c = 3072$ grid cells on the side, starting with initial conditions produced with the Zel'dovich approximation. Moreover, the cosmo-SLICS evolve a pair of simulations at each node, designed such as to suppress the sampling variance (see Harnois-Déraps et al. 2019, for more

details). Each cosmological model is ray-traced multiple times to produce 50 pseudo-independent light-cones of size 100 deg^2 .

For each realisation, we create KiDS-1000-like sources and KiDS-LRG-like lens catalogues, following the pipeline described in Harnois-Déraps et al. (2018); notably we reproduce exactly the source galaxy number density and $n(z)$ that is used in Asgari et al. (2021), who report a total number density $n_{\text{gal}} = 6.93/\text{arcmin}^2$ and a redshift distribution estimated from self-organising maps (see Wright et al. 2020). These mock galaxies are then placed at random angular coordinates on 100 deg^2 light-cones. In contrast to the T17 mocks, we test our model with two source redshift bins, corresponding to the KiDS-1000 fourth and fifth tomographic bins (hereafter z_s^{low} and z_s^{high}). The source galaxies are assigned a shear signal γ from a series of lensing maps, following the linear interpolation algorithm described in Sect. 2 in Harnois-Déraps et al. (2018).

For our lens sample, we opted to include only the second tomographic bin of the LRG galaxies described in Vakili et al. (2019). Compared to the T17, the $n(z)$ of the cosmo-SLICS LRG mocks have coarser redshift resolution of the simulations. Moreover, the $n(z)$ vary slightly for different underlying cosmologies, due to variations in the relation between co-moving distance and redshift. Following Vakili et al. (2019), we generate our LRG catalogues assuming a constant linear galaxy bias of 1.72, with a galaxy number density of $n_0 = 0.028 \text{ gal/arcmin}^2$. In Fig. 2 we show the target $n(z)$ of the galaxy samples with the solid lines, while the simulation $n(z)$ are displayed with the dashed lines.

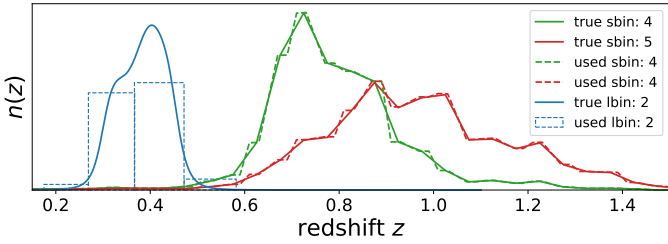


Fig. 2: Redshift distributions of the second LRG (lens) bin and the last two KiDS-1000 (source) bins (z_s^{low} and z_s^{high} , respectively). The continuous lines corresponds to the $n(z)$ of the real data, while the dashed lines belong to the mocks. The $n(z)$ are scaled such that a comparison is possible.

4.4. SLICS

In total the SLICS⁵ are a set of over 800 fully independent realisations similar to the fiducial ΛCDM cosmo-SLICS model. The underlying cosmological parameters for each run are the same, fixed to $\Omega_m = 0.2905$, $\Omega_\Lambda = 0.7095$, $\Omega_b = 0.0473$, $h = 0.6898$, $\sigma_8 = 0.826$ and $n_s = 0.969$ (see Hinshaw et al. 2013). For Fourier modes $k < 2.0 h \text{ Mpc}^{-1}$, the SLICS and cosmo-SLICS three-dimensional dark matter power spectrum $P(k)$ agrees within 2% with the predictions from the Extended Cosmic Emulator (see Heitmann et al. 2014), followed by a progressive deviation for higher k -modes (Harnois-Déraps et al. 2018). We use the SLICS to estimate a reliable covariance matrix, which, combined with the cosmo-SLICS, allows us to determine the validity regime of the model for different cosmologies. Similar to the T17 simulations, the signal of the SLICS

⁵ The SLICS are made publicly available on the SLICS portal at <https://slics.roe.ac.uk/>.

is combined with the randomly-oriented intrinsic shapes ϵ^s to create ellipticities, whereas ϵ^s is drawn from a Gaussian distribution with width σ_ϵ directly since the shear information are given here per galaxy. We added an additional layer of realism and used a redshift-dependent shape noise that better reproduces the data properties. Namely, we used $\sigma_\epsilon = 0.25$ and 0.27 for the source bins z_s^{low} and z_s^{high} , respectively, as reported in Giblin et al. (2020).

4.5. Extracting the SLICS and cosmo-SLICS data vector

The extraction of the data vector for the SLICS and cosmo-SLICS analyses is similar to the T17 case, where shape noise was not included for the cosmo-SLICS data vectors to better capture the cosmological signal. Another slight difference is that the light-cones are now square-shaped, which accentuates the edge effects when the aperture filter overlaps with the light-cone boundaries. One could in principle weight the outer rims for each N_{ap} map, such that the whole map can be used. Although this would increase our statistical power, it could also introduce a systematic offset. We opted instead to exclude the outer rim for each realization resulting in an effective area of $(10 - 2\Theta)^2 \text{ deg}^2$ with Θ the size of the corresponding filter. This procedure also ensures that roughly the same number of background galaxies are used to calculate the shear profile around each pixel.

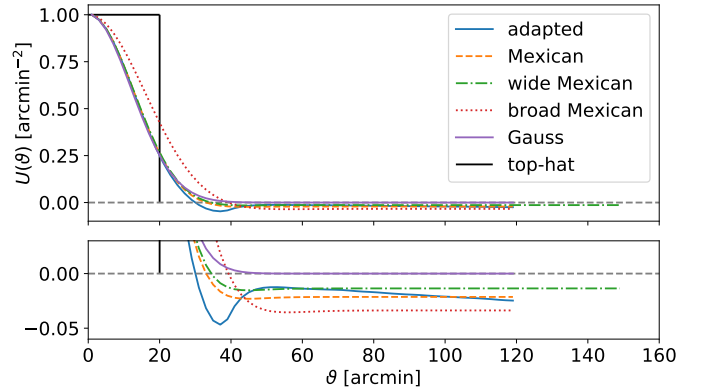


Fig. 3: Different filters U used in this work to verify the new model. For all filters we scaled the first bin value to $1/\text{arcmin}^2$ for comparison. The corresponding Q -filters are shown in Fig. C.1. The wide Mexican filter extends up to $150'$.

5. Testing the revised model

We use the simulations described in Sect. 4 to test our revised model and its accuracy in predicting shear profiles. Following the results of F18 we choose a top-hat filter of $20'$ as our starting point and we consider a number of more general filters with a similar angular extent, shown in Fig. 3. Our motivation for studying these filters is as follows: We use a Gaussian filter to test whether the model performs well for non-constant but positive filters; the ‘adapted’ filter is the filter that results from B20; the ‘Mexican’ filter removes the local minimum at $\vartheta \sim 40'$; the ‘broad Mexican’ has a larger width; finally the ‘wide Mexican’ suppresses the negative tail. In order to lower the amplitude of the negative part while keeping a similar width, we adjusted the upper bound of the wide-Mexican filter to conserve the compensation to $150'$, which makes it better suited to large contiguous survey areas.

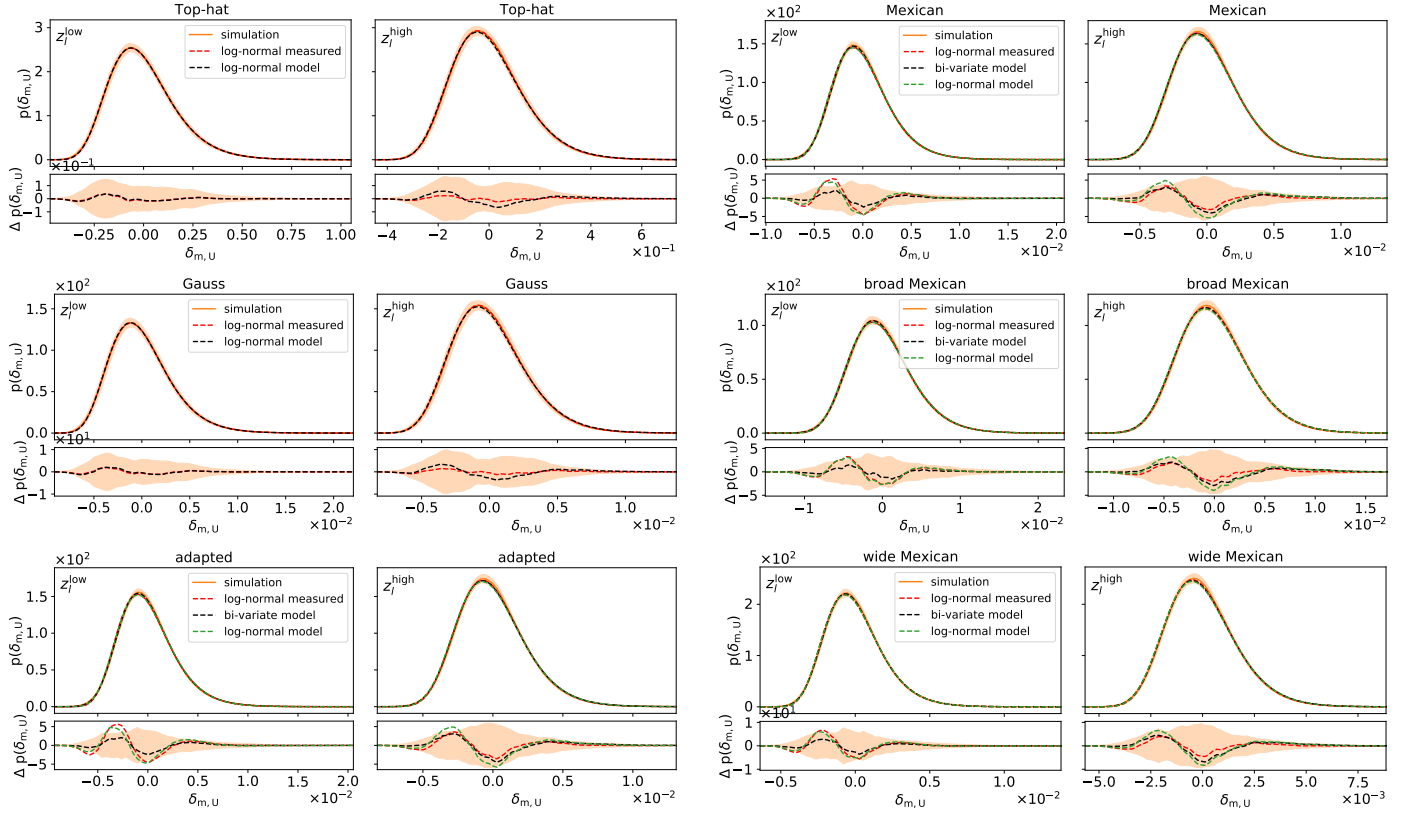


Fig. 4: PDF of $\delta_{m,U}$ smoothed with the filters shown in Fig. 3. The orange shaded region is the standard deviation of 48 sub-patches scaled by a 777.4/859.4 to mimic the KiDS-1000 footprint. The red dashed curve corresponds to a log-normal PDF with the measured moments from the smoothed density maps, and indicates the accuracy using a log-normal PDF. The green and the black dashed lines are both from the model, where the green corresponds to the PDF of $\delta_{m,U}$ when using log-normal and the black dashed using the bi-variate approach described in Eq. (26). The lower panels show the residuals $\Delta p(\delta_{m,U})$ of all lines with respect to the simulations.

Before comparing our model to the simulations, we note that we are using here the revised model even for the top-hat filter, for which we could instead use the F18 model directly. Notably, the derivations of $\langle \delta_{m,U}^2 \rangle$ and $\langle \delta_{m,U}^3 \rangle$ are identical in the revised model, and we show in the following plots for the top-hat filters that both models yield almost identical results in predicting the shear profiles with a top-hat filter. Therefore, from here on, we only show results from the revised model. In the following three sections, we validate the key model ingredients introduced in Sect. 3.1- 3.3.

5.1. Validating $p(\delta_{m,U})$

We show in Fig. 4 the PDF of the smoothed two-dimensional density contrast for all six filters, and for the two lens bins. In each case, we show with the orange shaded region the 1σ region measured from the 48 sub-patches extracted from one of the T17 simulations. In order to match the statistical precision of the KiDS-1000 data, we area re-scale the error bars by a factor $\sqrt{777.4/859.4}$, where 777.4 deg^2 is the effective survey area of KiDS-1000 (see Giblin et al. 2020). With the black dashed curve the fiducial model predictions is shown, and the red dashed curve is a log-normal PDF with the measured $\langle \delta_{m,U}^2 \rangle$ and $\langle \delta_{m,U}^3 \rangle$ from the T17 simulations and indicates whether the true distribution follows a log-normal distributed. For the compensated filters, we additionally show with the green dashed curves the case where we used a single log-normal distribution (as opposed to our bi-variate model) as it is done for the positive filters introduced in

Sect. 3.1. We see by inspecting the different panels that the predictions agree with the simulations for the two lens bins within 1σ cosmic variance expected for KiDS-1000. We note here that this PDF cannot be measured in real data, and that the real test for the accuracy of our model are the shear signals, with larger uncertainties due to shape-noise. Nevertheless, for the top-hat and the Gaussian we have an agreement between model and simulation well within the 1σ , which indicates that the log-normal approximation for these filters is good. The other filters show stronger deviations when using a log-normal approximation, but these are weaker when the negative part of the filter approaches zero (wide Mexican) or when width of the filter increases (broad Mexican), although the negative part of the broad Mexican is stronger than for the Mexican filter. This indicates that probing on larger scales either with a broader or wider filter the log-normal approximation is more accurate. Furthermore, when using the bi-variate log-normal approach discussed in Sect. 3.1, the residuals are even more suppressed, such that we cannot recognise differences in the match between predicted and measured PDF for all compensated filters. Although the model for the compensated filters is not as good as for the non-negative filters (top-hat and Gaussian), the revised model remains throughout consistent with the T17 simulations.

5.2. Validating $p(N_{\text{ap}})$

We next show in Fig. 5 how well the model can predict $p(N_{\text{ap}})$ given the galaxy distributions described in Sect. 4. As for

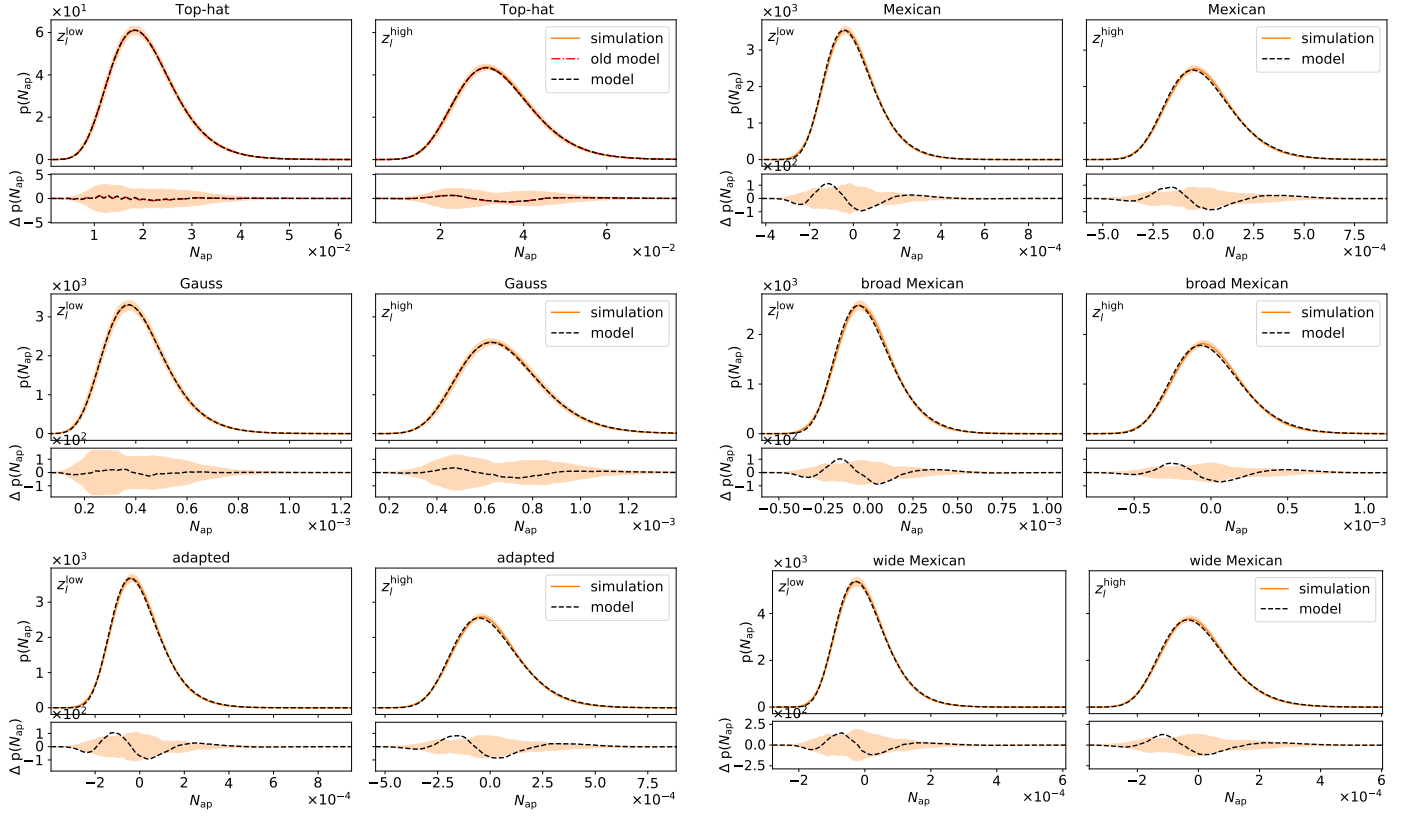


Fig. 5: PDF of N_{ap} calculated with the filters U in Fig. 3. The orange lines are determined with the simulations and the orange shaded region is the standard deviation from 48 sub-patches. The black dashed lines corresponds to the results from the new model, and for comparison the red dashed line in the upper left panel is from the old model. The lower panels show the residuals $\Delta p(N_{\text{ap}})$ of all lines with respect to the simulations.

$p(\delta_{\text{m},U})$, the best matches are observed for the non-negative filters, where the simple log-normal PDF is used. For the compensated filters with the bi-variate log-normal $p(\delta_{\text{m},U})$ we notice a slight deviation in the skewness of $p(N_{\text{ap}})$. These discrepancies are not seen when placing galaxies at random positions regardless of any underlying matter density field as shown in Fig. A.1, which indicates that they must originate either from $p(\delta_{\text{m},U})$ or from the $\langle w_{\theta} | \delta_{\text{m},U} \rangle$ term (we set the latter to 0 for uniform random fields). It might be that the deviations seen in $p(N_{\text{ap}})$ are exclusively caused by the deviations in $p(\delta_{\text{m},U})$, but since they are much smaller, we expect that the assumptions made in computing $\langle w_{\theta} | \delta_{\text{m},U} \rangle$ induce additional inaccuracies. Nevertheless, we will see next that these deviations result in shear signals whose residuals are well within the statistical uncertainties of Stage-III weak lensing surveys such as KiDS-1000. However the accuracy of the $\langle w_{\theta} | \delta_{\text{m},U} \rangle$ term will likely need to be improved for future surveys like *Euclid*, as discussed in Sect. 3.2.

5.3. Validating $\langle \gamma_i | Q \rangle$

Having quantified the accuracy of the basic ingredients of our model, we are now in a position to compare the predicted and measured shear profiles. This is the main result of our paper, which is shown in Fig. 6. Following G18, we use five quantiles and we measure the shear profiles up to 120' (or 150' for the wide Mexican case). Once again, the orange shaded region shows the standard deviation measured from the T17 simulations, scaled to the KiDS-1000 area. For the top-hat, Gaussian and wide Mexican filter, we see no significant deviations between the model and the simulations. For the other three cases, the shear profiles

show minor discrepancies in some quantiles and at large angular scales, but always consistent and within the KiDS-1000 accuracy. The shapes of the signals are affected by the choice of filter: we can observe shifts in the peak positions and changes in the slope of the signals especially at small scales. This allows us in the next section to select filters that optimise the signal-to-noise of the measurement while being clean of systematics related to small-scale inaccuracies.

5.4. Quantifying the model accuracy

We benchmark the accuracy of our model by a χ^2 -minimisation and estimate the uncertainty by means of a Fisher matrix. This will test how well the true cosmology can be recovered given the residual discrepancies between our model and the measurements in the T17 simulations. In our first analysis we test three different data compression techniques, where two of them compress the signal into an aperture mass value given by Eq. (4). Therefore we are limited in this first analysis to the compensated filters, for which Q -filter are derivable with Eq. (5). This analysis setup is labelled with ' M_{ap} ' and uses exclusively the aperture mass values. This setup has the benefit of a strong data compression, at the cost of losing some cosmological information contained in the shape of the profiles. Notably, the slope of the profiles at large angles is connected to the two-halo terms, which in turn is sensitive to Ω_{m} . We therefore consider a second case, hereafter ' $M_{\text{ap}} + S$ ', where we combine the aperture mass (4) with the slope of the shear profiles beyond the maximum for the positive γ_1 and the minimum for the negative γ_1 . More precisely, the slope is measured with a linear regression, including ϑ -bins from the

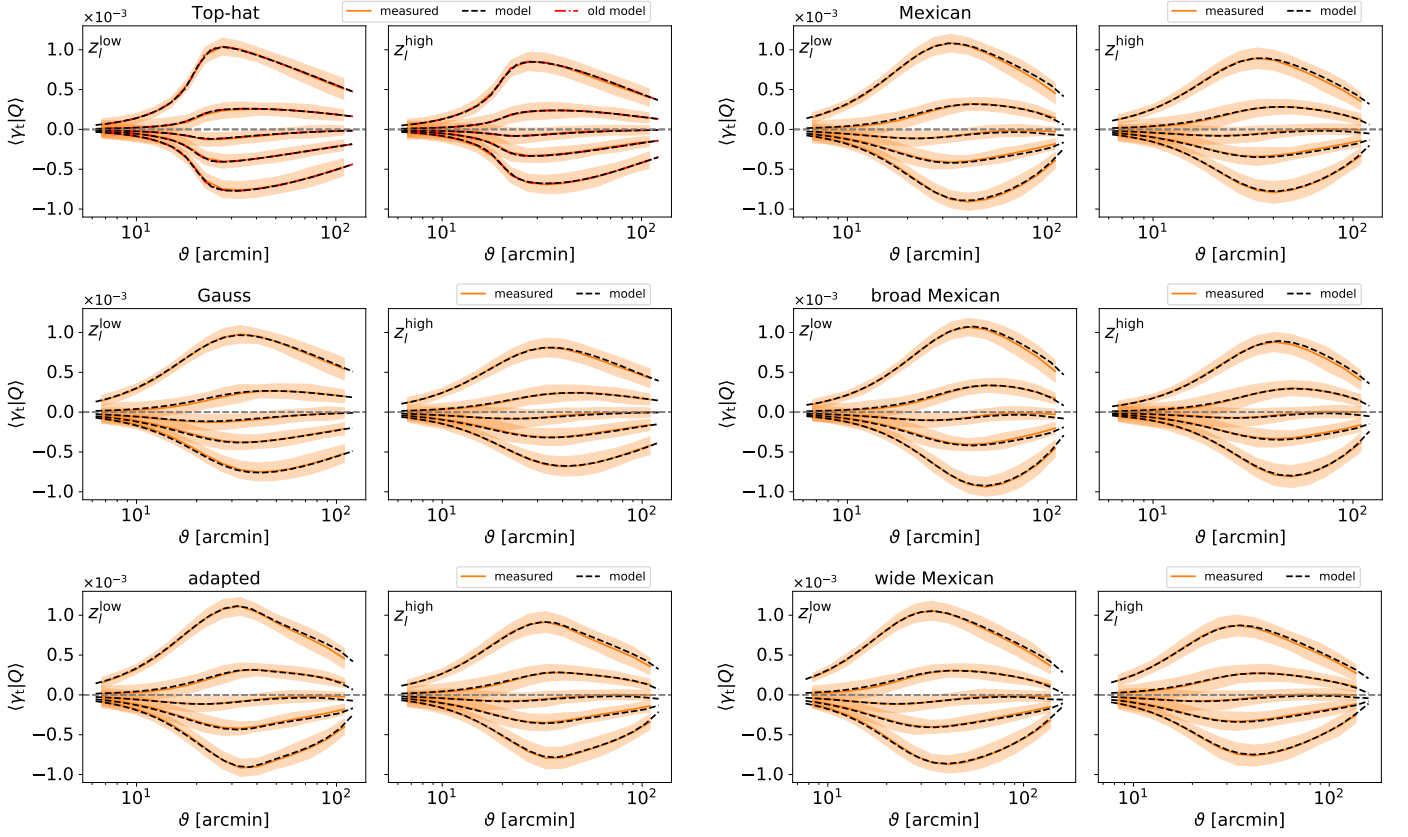


Fig. 6: Predicted shear profiles for the two adapted filters shown in the dashed black line and measured shear profiles shown in orange for the new model with filter U . The orange shaded region is the standard deviation on the mean from 48 sub-patches.

peak of γ_t in each quantile to maximum θ . Finally, our last analysis setup, which we label with ' F ', uses the full shear profiles from Fig. 6 as our data and model. As it was shown in F18 that the model is not fully accurate for small angular scales, we make a conservative cut and include only scales above $14''$.⁶ For the comparison between the three setups (M_{ap} , $M_{ap} + S$ and F) we decided to use the adapted filter.

Since the mean aperture mass summed over all quantiles vanishes per definition, one of the five shear signals is fully determined by the others, such that we decided to neglect for all three cases the middle quantile with lowest signal. Thus, we end up with data and model vectors of size 8, 16 and 88 for the M_{ap} , $M_{ap} + S$ and F setups, respectively. As explained previously, we measure our covariance matrix from our ten T17 simulations, each divided into 48 sub-patches, for a total of 480 sub-patches. We note here that the galaxy number density can slightly deviate between the different realizations due to the Poisson sampling, but these are inevitable anyway due the splitting in sub-patches. Given the amplitude of these small fluctuations, these can be safely neglected. For all three cases we de-bias the inverse covariance matrix C^{-1} following Hartlap et al. (2007),

$$C^{-1} = \frac{n - p - 2}{n - 1} \hat{C}^{-1}, \quad (45)$$

where n is the number of simulations (480) and p the size of the data vector (8, 16, or 88). Finally, given our data \mathbf{d} measured from only one noise-free T17 realization, and our model vector

\mathbf{m} , we measure for the three cases the χ^2 statistics as

$$\chi^2 = [\mathbf{m} - \mathbf{d}]^T C^{-1} [\mathbf{m} - \mathbf{d}], \quad (46)$$

which we then minimise by varying the input cosmology in the model. If the model was perfect, the best-fit cosmology would align exactly with the truth within the negligible statistical uncertainties of the simulations, hence this exercise allows us to track any biases in the inferred cosmology these residuals may cause.

With the fixed covariance C and assuming a Gaussian likelihood, the Fisher matrix can be computed as (Tegmark et al. 1997)

$$F_{ij} = \left(\frac{\partial \mathbf{m}(\boldsymbol{\pi})}{\partial \pi_i} \right)^T C^{-1} \left(\frac{\partial \mathbf{m}(\boldsymbol{\pi})}{\partial \pi_j} \right), \quad (47)$$

where $\boldsymbol{\pi} = (\Omega_m, \sigma_8)^T$ contains the cosmological parameters that are varied. The partial derivatives are calculated numerically with a five-point stencil approximation as (Fornberg 1988)

$$\frac{\partial \mathbf{m}(\boldsymbol{\pi})}{\partial \pi_i} \approx \frac{-\mathbf{m}(\pi_i + 2\Delta\pi_i) + 8\mathbf{m}(\pi_i + \Delta\pi_i) - 8\mathbf{m}(\pi_i - \Delta\pi_i) + \mathbf{m}(\pi_i - 2\Delta\pi_i)}{12\Delta\pi_i}, \quad (48)$$

where we found that with steps $\Delta\pi = 0.02\pi$ the derivatives are accurate enough without being sensitive to numerical noise. Under the assumptions that the vector \mathbf{m} is drawn from a multivariate Gaussian distribution and its dependence on the parameters $\boldsymbol{\pi}$ is close to linear (Trotta 2017; Uhlemann et al. 2020),

⁶ We also repeated the analysis on the full signal, which resulted in the same constraining power.

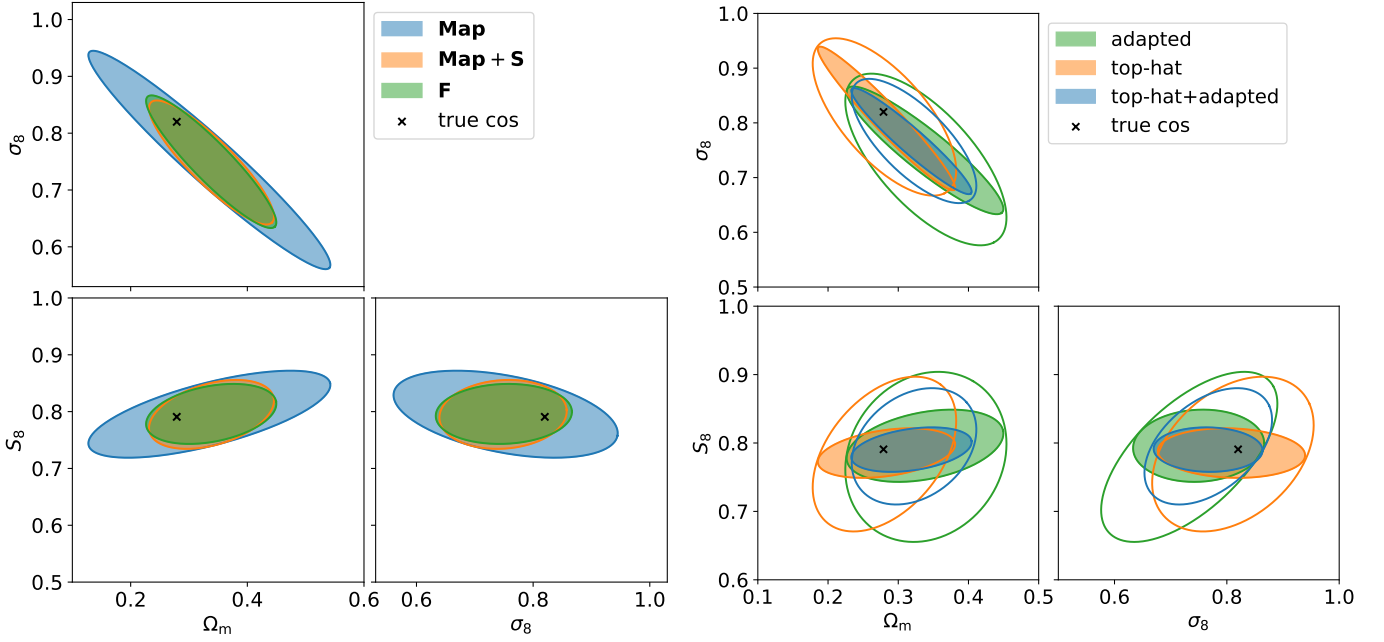


Fig. 7: The $1\text{-}\sigma$ confidence region around the best-fit cosmology. On the left, the contours resulting from the three different data compression techniques for the adapted filter are shown. The first technique uses only information about the amplitude of the shear profiles (M_{ap}); the second combines this amplitude with the slope of the shear profiles beyond the peak ($M_{\text{ap}} + S$); and the third uses the full shear profile above $14''$ without compression (F). On the right, we show the $1\text{-}\sigma$ confidence region placed around the best-fit cosmology with the third technique (F) when using the shear profiles resulting from the adapted filter alone, the ones resulting from the top-hat filter alone, and when concatenating the shear profiles of both filters. The filled contours show the constraints for the fixed biases and the open contours for the marginalised galaxy biases. Note that the green contour on the left is the same as the filled green contour on the right.

the parameter covariance matrix C_π is given by the inverse of the Fisher matrix. Although this statement is generally true only at the fiducial π , we use the fact that for a near-linear model the full posterior can be approximated by a Gaussian with covariance C_π . In the left panel of Fig. 7 we display the $1\text{-}\sigma$ confidence region for the adapted filter for all three cases around their best-fit cosmologies. We observe that for the three cases, the input cosmology lies within the $1\text{-}\sigma$ contour, with a tendency towards higher Ω_m and lower σ_8 values. These deviations are reported in Table 1, where we also show that there is only a negligible bias with respect to S_8 , which indicates that our model can be safely used for the analysis of Stage-III weak lensing data where typically the focus is on that particular parameter combination. Comparing the three different methods, we can see that using information about the slope of the profiles (model $M_{\text{ap}} + S$) increases drastically our constraints perpendicular to the S_8 direction.

Table 1: Overview of the best-fit cosmology with the constraining power that we get with the adapted filter for the three different methods we applied. The constraints here follow from the inverted Fisher matrix around the best-fit cosmology, where the input cosmology is $\Omega_m = 0.279$, $\sigma_8 = 0.820$ and thus $S_8 = \sigma_8 \sqrt{\Omega_m/0.3} = 0.791$.

	Ω_m	σ_8	S_8
M_{ap}	0.335 ± 0.137	0.753 ± 0.127	0.795 ± 0.051
$M_{\text{ap}} + S$	0.339 ± 0.071	0.748 ± 0.072	0.795 ± 0.040
F	0.338 ± 0.074	0.750 ± 0.077	0.796 ± 0.035

Since the best constraints with the lowest systematic bias results when using the full signal F , we repeat the analysis with the full signal for all filters and show the constraining power in Table 2, where it is seen that the analysis with the Gaussian and

the top-hat filter results in almost no systematic bias. The compensated filters in turn have a bias in Ω_m and σ_8 , but it is smaller than the expected KiDS-1000 uncertainty.

As a final investigation, we explore the possibility of increasing our constraining power by combining the full shear profiles F from two different U filters, those resulting from the adapted filter and the top-hat filter. In right panel of Fig. 7 we display the $1\text{-}\sigma$ confidence region for the separate filters and the combination for the F case. Note that the green contour in the right panel corresponds to the F contour presented in left panel of Fig. 7. Combining the two filters has a small impact on S_8 , but results in a significant improved constraining power on Ω_m and σ_8 separately, as shown in Table 2.

In the results presented so far, we only varied Ω_m and σ_8 , and kept all other parameters fixed. In particular, the two galaxy bias parameters were set to their input value; however, such information is not available in real data. We therefore relax this assumption now and allow the constant linear galaxy biases b to vary as well. The $1\text{-}\sigma$ confidence intervals after marginalisation over the constant linear galaxy biases of the two lens samples with flat wide priors are stated in the lower part of Table 2. In an actual data analysis, we might be able to include some informative prior on the bias, for example from clustering measurement of the foreground lenses, hence this current case can be viewed as an upper limit on the effect of bias marginalisation. As expected, the confidence intervals become significantly larger in this process, but more importantly the inferred best-fit cosmology does not move further away from the truth. When comparing the upper and lower sections of Table 2, we observe that marginalising over the galaxy biases has no impact on Ω_m , some on σ_8 , but significantly degrades the precision on S_8 . This arises due to a degeneracy between S_8 and the galaxy bias parameters, which

both modulate the amplitude of the shear signal. Assuming wide flat priors is therefore not the optimal approach, and one should for instance instead include information on the biases b from the lens clustering, or as G18 from the PDF of N_{ap} .

Table 2: Overview of the best-fit cosmology with the constraining power that we get for the \mathbf{F} vectors for all filters. In the lower part we marginalise over the biases b for the adapted, Gaussian and the combined data vector. The values here follow from the inverted Fisher matrix around the best-fit cosmology, where the input cosmology is $\Omega_m = 0.279$, $\sigma_8 = 0.820$ and thus $S_8 = \sigma_8 \sqrt{\Omega_m}/0.3 = 0.791$. Furthermore, we note that the parameter uncertainties increase slightly if we also vary parameters like the time-independent equation-of-state parameter of dark energy w_0 or the scalar spectral index n_s .

fixed b	Ω_m	σ_8	S_8
wide M.	0.327 ± 0.078	0.759 ± 0.086	0.792 ± 0.033
broad M.	0.336 ± 0.078	0.748 ± 0.087	0.791 ± 0.039
Mexican	0.343 ± 0.076	0.742 ± 0.079	0.793 ± 0.035
Gaussian	0.274 ± 0.059	0.815 ± 0.098	0.780 ± 0.034
adapted	0.338 ± 0.074	0.750 ± 0.077	0.796 ± 0.035
top-hat	0.283 ± 0.065	0.808 ± 0.087	0.785 ± 0.024
ad.+th.	0.319 ± 0.057	0.767 ± 0.064	0.790 ± 0.022
marg. b			
adapted	0.339 ± 0.076	0.733 ± 0.102	0.780 ± 0.079
top-hat	0.280 ± 0.068	0.811 ± 0.095	0.784 ± 0.075
ad.+th.	0.323 ± 0.059	0.767 ± 0.075	0.795 ± 0.056

In order to compare our results with G18, who derived constraints of $\Omega_m = 0.26^{+0.04}_{-0.03}$ and $S_8 = 0.90^{+0.10}_{-0.08}$ with their fiducial analysis, we need to multiply our uncertainty intervals by $\sqrt{777.4/1321}$, to account for the smaller area of KiDS-1000 (777.4 deg^2) compared to the DES Y1 area (1321 deg^2). Furthermore, we exclusively used information about the shear profiles, whereas G18 also used the mean aperture number in each quantile. We are somewhat sceptical about using the aperture number here or in future analysis for the compensated filters, because we have significant residual discrepancies between model and simulation, which would strongly affect our analysis. The match of the shear profiles in turn is very accurate in our simulations, which shows that they are robust against uncertainties in $P(N_{\text{ap}})$. For instance, if one monotonically transforms the N_{ap} values, the predicted $P(N_{\text{ap}})$ would change, but the segmentation into quantiles would not be affected, hence the shear profiles remain the same. Another advantage of not using $P(N_{\text{ap}})$ is that we do not need to model shot noise in the galaxy distribution. However, for the Gaussian and the top-hat filter the predicted $P(N_{\text{ap}})$ match the measured one, and since F18 and G18 have shown that the model is accurate for the top-hat, even when the galaxies are not placed with linear bias and shot-noise by hand, it could help to include $P(N_{\text{ap}})$ information for the non-compensated filters. Nevertheless, we see that our constraints from using only information about the shear profiles can be similar as the ones in G18.

5.5. Validating the model for different cosmologies

In this section we aim to determine the validity regime of our model in a wider cosmological parameter space. For this purpose we use the cosmo-SLICS simulations with their 26 different w CDM cosmologies. Since we already established above that the model performs well for a Λ CDM cosmology, we concentrate here on the comparison between the measured shear profiles for each of these 26 different cosmologies and the predicted shear profiles from the model at that specific cosmology. We use

the shear profiles measured through the Gaussian filter and the adapted filter in order to validate the model also for a compensated filter. As described in Sect. 4, this analysis consists of only one lens bin and two source bins.

Before turning to different cosmologies, we show that our model also fits the fiducial model in cosmo-SLICS, showing the agreement between them and the Takahashi simulation. Hence, we show for both filters the measured and predicted PDF of N_{ap} in Fig. 8 and the corresponding shear profiles in Fig. 9 for the fiducial cosmology. The slightly worse match for the cosmo-SLICS could be caused by edge effects (contiguous full-sky vs. 100 deg^2 patches), the smaller statistic (41253 deg^2 vs. 5000 deg^2), or the choice of the matter power spectrum $P(k)$ that is used in the model. Indeed, we use the Takahashi et al. (2012) HALOFIT function throughout this paper, which is calibrated on the same N -body code that is used to create the T17 simulations (Springel et al. 2001, GADGET2), and which is known to have an excess power of 5-8% in the mildly non-linear regime (Heitmann et al. 2014). The SLICS and cosmo-SLICS, in contrast, are produced from CUBEP³M (Harnois-Déraps et al. 2013), whose $P(k)$ agrees better with the Cosmic Emulator of Heitmann et al. (2014). Nevertheless the match between the model and the cosmo-SLICS simulations is accurate enough for this work, and we keep further investigation on the impact of $P(k)$ choices for future work.

Finally, to quantify the accuracy of the model for a wide range of cosmological parameters, we repeat the exercise done in the last section, i.e. computing the χ^2 defined in Eq. (46) by using the full shear signal above $14'$ (\mathbf{F}), which results again in a data vector \mathbf{d} of size 88 (four quantiles \times two source bins \times 11 angular bins), and additionally using only information about the amplitude of the shear profiles (\mathbf{M}_{ap}) with data vector \mathbf{d} of size 8 (four quantiles \times two source redshift bins). Since we are limited for \mathbf{M}_{ap} to compensated filters, we perform the comparison for \mathbf{M}_{ap} only for the adapted filter, whereas for the \mathbf{F} method we use the adapted and the Gaussian filter. In order to estimate the expected χ^2 values for the KiDS-1000 survey with an area of 777.4 deg^2 we averaged shear profiles with shape noise from eight of the 50 realization per cosmology, such that we ended up with six χ^2 values per cosmology node. Furthermore, for the first \mathbf{F} method we used a cosmology-independent covariance matrix estimated from 700 SLICS realisations, in which the shape noise is included. In contrast, for the \mathbf{M}_{ap} method, which has a data vector of only 8 elements, we are able to calculate a reliable cosmology-dependent covariance matrix from the 50 realizations from each cosmology. The inverse covariance matrix is corrected with Eq. (45) and the covariance is re-scaled to the KiDS-1000 area. The results for both methods are shown in Fig. 10, which shows the dependence of the mean of the six χ^2 values on the Ω_m and σ_8 value of that node. We note here that although not indicated in Fig. 10 the time-independent equation-of-state parameter of dark energy w_0 and the dimensionless Hubble parameter h are also different in each cosmology, as can be seen in Table C.1. But since we found that they are uncorrelated with the χ^2 values we did not study their dependence in our investigation.

To decide next for which cosmologies the predicted and measured shear profiles are in accordance, we determined those χ^2 values which correspond to a p -value of 1% and 10%, and plot them as the grey dashed lines in Fig. 10. These lower limits help us to decide for which cosmology the null hypothesis that the model predicts the correct shear signals can be rejected. As shown in Fig. 10, the null hypothesis can be rejected only for the adapted filter for the lowest Ω_m and highest σ_8 . In models with

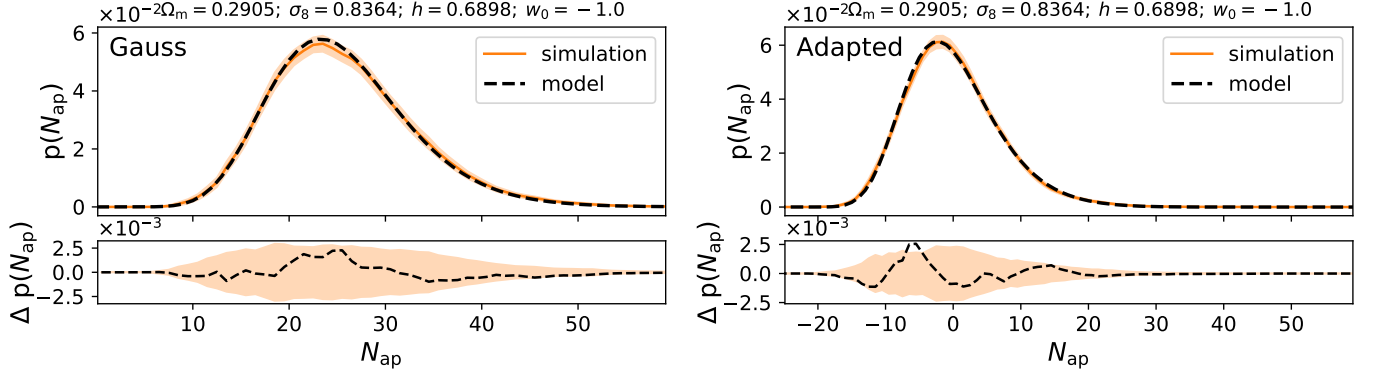


Fig. 8: PDF of the aperture number for the fiducial cosmology in cosmo-SLICS with the Gaussian filter on left and the adapted filter on the right side. The orange shaded region is the standard deviation of the 50 realizations given for each cosmology divided by $\sqrt{777.4/100}$ to mimic the KiDS-1000 footprint. The lower panels show the residuals $\Delta p(N_{\text{ap}})$ of the model with respect to the simulations.

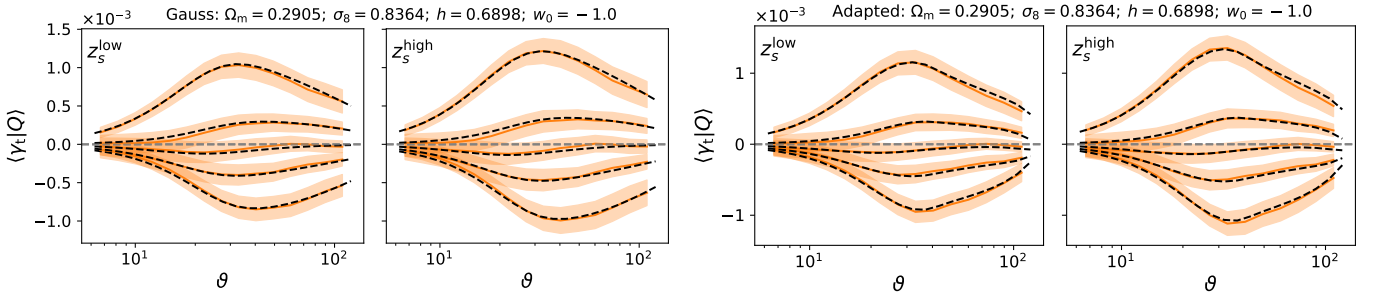


Fig. 9: Resulting shear profiles for the Gaussian filter on the left and for the adapted filter on the right side of the fiducial cosmology in cosmo-SLICS. The orange shaded region is the standard deviation from 700 SLICS realizations with shape-noise divided by $\sqrt{777.4/100}$ to mimic the KiDS-1000 footprint. The orange lines are the mean shear profiles from the 50 realization per node without shape noise.

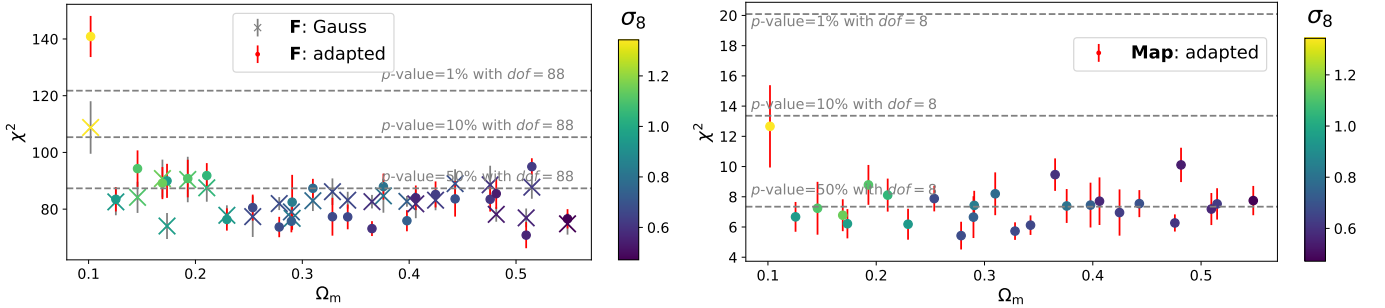


Fig. 10: Resulting mean χ^2 in relation to the Ω_m and σ_8 (colour) values. The mean of each χ^2 value results from six χ^2 values per cosmological model, which in turn are measured from the average of eight shear profiles with shape noise. In the left panel the χ^2 values are determined from the full shear signal above $14'$ (F) with a cosmology-independent covariance matrix, and the ones in the right panel from the amplitude of the shear profiles (M_{ap}) with a cosmology-dependent covariance matrix. The error bars correspond to the error on the mean from the six values. The grey dashed lines are those χ^2 values for which the p -values are 50%, 10% and 1%, and therefore indicate the mean limits to find χ^2 that are larger. Although not indicated, the time-independent equation-of-state parameter of dark energy w_0 and the dimensionless Hubble parameter h are also varied in each cosmology and can be seen in Table C.1, but since they are basically uncorrelated to the χ^2 values we ignore them here.

these extreme cosmological parameters the density field will be very non-linear today (high σ_8) and it will have been non-linear for a longer time (low Ω_m means that structure grows slower, i.e. decreases slower as one goes to higher redshifts). Both of these features will decrease the accuracy of many of our modelling assumptions, and since more and stronger assumptions are made for the compensated filters, it is less accurate in these highly non-linear regimes. However, such extreme cosmologies are disfavoured by current cosmic shear data analyses (see e.g. Asgari

et al. 2021; Heymans et al. 2021), hence should not cause any problem in future analyses based on density split statistics.

6. Summary and conclusion

In our previous work (Burger et al. 2020) we showed that using compensated filters in the density split statistic (DSS) to quantify over- and under-dense regions on the sky have advantages compared to the top-hat filter, both in terms of the overall signal S/N and in recovering accurately the galaxy bias term. Gruen et al.

(2016) demonstrated that the DSS is a powerful cosmological tool, by constraining cosmological parameters with DSS measurements from the Dark Energy Survey (DES) First Year and Sloan Digital Sky Survey (SDSS) data, using the DSS model derived in Friedrich et al. (2018) which uses a top-hat filter. They found for the matter density parameter $\Omega_m = 0.26^{+0.04}_{-0.03}$, a constraint that agrees and is competitive with the DES analysis of galaxy and shear two-point functions (see Abbott et al. 2018).

Following these previous works we modify the model of Friedrich et al. (2018) in such a way that it can predict the shear profiles $\langle \gamma_i | Q \rangle$ for a given quantile Q of the aperture number N_{ap} for general filters (Gaussian and also compensated filters). This is achieved by recalculating the three basic ingredients, which are the PDF of the projected matter density contrast smoothed with the filter function, $p(\delta_{m,U})$, the expectation value of the convergence inside a radius ϑ for a fixed smoothed matter density contrast, $\langle \kappa_{<\vartheta} | \delta_{m,U} \rangle$, and the distribution of N_{ap} for the given filter function U given the smoothed matter density contrast $p(N_{\text{ap}} | \delta_{m,U})$. While for $\langle \kappa_{<\vartheta} | \delta_{m,U} \rangle$ we modified the calculation of the moments for general filters, we introduced new approaches to calculate $p(N_{\text{ap}} | \delta_{m,U})$ and $p(\delta_{m,U})$ for compensated filters. While for non-negative filters, $\delta_{m,U}$ is well described by a log-normal PDF, we found significant deviations for compensated filters. To solve this issue we used a bi-variate log-normal ansatz, where we assumed that $\delta_{m,U}$ can be divided into two log-normal random variables with each separately following a log-normal distribution. For the calculation of $p(N_{\text{ap}} | \delta_{m,U})$ we derived an expression for the corresponding characteristic function, which can be used either directly to calculate $p(N_{\text{ap}} | \delta_{m,U})$ by inverse Fourier transformation or by calculating the first three moments which then specify a log-normal distribution for $p(N_{\text{ap}} | \delta_{m,U})$. The differences between these two approaches are considerably smaller than the statistical uncertainty, such that we used the latter approach because of its smaller computational time.

In order to validate the revised model, we compared it to two independent sets of simulations. For this purpose we used the of simulations Takahashi et al. (2017) for general and detailed comparison, and the cosmo-SLICS (Harnois-Déraps et al. 2019) to determine the dependence on cosmological parameters. For non-negative filters like a top-hat or a Gaussian, no significant difference between model and simulations for the PDF or the tangential shear profiles was detected. For compensated filters, we found some discrepancies in the predicted PDF of N_{ap} and shear signals. However, we also noticed that we can minimise these deviations by decreasing the negative weight of the filter U . All these differences are much smaller than the statistical uncertainties for Stage-III surveys like KiDS-1000.

Finally, to benchmark the accuracy of our model we performed a χ^2 minimisation process and estimated the uncertainties by means of the Fisher matrix. This allowed us to test how well the true cosmology can be recovered given the residual discrepancies. In this analysis we ascertained that the compensated filters tend to prefer smaller σ_8 and higher Ω_m , but S_8 was almost perfectly recovered. Hence we conclude to have no systematic offset in the parameter that weak lensing is most sensitive to. We also checked whether the model is stable for different cosmologies. For this we modeled shear profiles for all 26 cosmologies in cosmo-SLICS. For models with $\sigma_8 > 1$, the deviation between model and simulations are significant, in particular for the adapted filter. Nevertheless we are not concerned about this fact, because current weak lensing analyses show that this parameter space is strongly disfavoured. Lastly we forecast the constraining power that we can expect, by combining the shear information from an adapted and a top-hat filter. In our

best-case scenario, when varying only σ_8 and Ω_m , we found an uncertainty on $S_8 = \pm 0.02$. Furthermore, we discovered that the deviation for the compensated filters can be largely corrected by leaving the galaxy biases as free parameters, which will be done in future analysis anyway due to the uncertainty in the measured biases.

After passing all these tests, we are confident that the revised model can be readily applied to Stage-III lensing data. We note that a number of systematic effects related to weak lensing analyses will require external simulations, notably regarding the inclusion of secondary signal from the intrinsic alignments of galaxies, or from the impact of baryonic feedback on the matter distribution. However, our model is well suited to capture the uncertainty about the lens and source redshift distribution, the shape calibration bias, or the galaxy bias, at a low computational cost, and is therefore ideally suited to perform competitive weak lensing analyses in the future.

Acknowledgements. This paper went through the whole KiDS review process, where we especially want to thank the KiDS-internal referee Benjamin Joachimi for his fruitful comments to improve this work. Further, we would like to thank Mike Jarvis for maintaining TREECORR and Ryuichi Takahashi for making his simulation suite publicly available. PB acknowledges support by the Deutsche Forschungsgemeinschaft, project SCHN342-13. OF gratefully acknowledges support by the Kavli Foundation and the International Newton Trust through a Newton-Kavli-Junior Fellowship and by Churchill College Cambridge through a postdoctoral By-Fellowship. JHD is supported by a STFC Ernest Rutherford Fellowship (project reference ST/S004858/1). Author contributions: all authors contributed to the development and writing of this paper.

References

- Abbott, T. M. C., Abdalla, F. B., Alarcon, A., et al. 2018, *Phys. Rev. D*, 98, 043526
- Abramowitz, M. & Stegun, I. A., eds. 1972, *Applied mathematics series*, Vol. 55, *Handbook of mathematical functions with formulas, graphs, and mathematical tables*, 10th edn. (Washington, DC: US Government Printing Office)
- Asgari, M., Lin, C.-A., Joachimi, B., et al. 2021, *A&A*, 645, A104
- Barthelemy, A., Codis, S., & Bernardeau, F. 2021, *MNRAS*, 503, 5204
- Bergé, J., Amara, A., & Réfrégier, A. 2010, *ApJ*, 712, 992
- Bernardeau, F., Colombi, S., Gaztañaga, E., & Scoccimarro, R. 2002, *Phys. Rep.*, 367, 1
- Bernardeau, F. & Valageas, P. 2000, *A&A*, 364, 1
- Boyle, A., Uhlemann, C., Friedrich, O., et al. 2020, arXiv:2012.07771
- Burger, P., Schneider, P., Demchenko, V., et al. 2020, *A&A*, 642, A161
- DeRose, J., Wechsler, R. H., Becker, M. R., et al. 2019, arXiv:1901.02401
- DES Collaboration, Abbott, T. M. C., Aguena, M., et al. 2021, arXiv e-prints, arXiv:2105.13549
- Eisenstein, D. J. & Hu, W. 1998, *ApJ*, 496, 605
- Euclid Collaboration, Knabenhans, M., Stadel, J., et al. 2020, arXiv:2010.11288
- Fan, Z., Shan, H., & Liu, J. 2010, *ApJ*, 719, 1408
- Fornberg, B. 1988, *Math. Comp.*, 184, 699–706
- Friedrich, O., Gruen, D., DeRose, J., et al. 2018, *Phys. Rev. D*, 98, 023508
- Fu, L., Kilbinger, M., Erben, T., et al. 2014, *MNRAS*, 441, 2725
- Giblin, B. et al. 2020, arXiv:2007.01845
- Gruen, D., Friedrich, O., Amara, A., et al. 2016, *MNRAS*, 455, 3367
- Gruen, D., Friedrich, O., Krause, E., et al. 2018, *Phys. Rev. D*, 98, 023507
- Halder, A., Friedrich, O., Seitz, S., & Varga, T. N. 2021, arXiv:2102.10177
- Hamana, T., Shirasaki, M., Miyazaki, S., et al. 2020, *PASJ*, 72, 16
- Harnois-Déraps, J., Amon, A., Choi, A., et al. 2018, *MNRAS*, 481, 1337
- Harnois-Déraps, J., Giblin, B., & Joachimi, B. 2019, *A&A*, 631, A160
- Harnois-Déraps, J., Martinet, N., Castro, T., et al. 2020, arXiv:2012.02777
- Harnois-Déraps, J., Pen, U.-L., Iliev, I. T., et al. 2013, *MNRAS*, 436, 540
- Hartlap, J., Simon, P., & Schneider, P. 2007, *A&A*, 464, 399
- Heitmann, K., Lawrence, E., Kwan, J., Habib, S., & Higdon, D. 2014, *ApJ*, 780, 111
- Heymans, C., Tröster, T., Asgari, M., et al. 2021, *A&A*, 646, A140
- Hilbert, S., Hartlap, J., & Schneider, P. 2011, *A&A*, 536, A85
- Hinshaw, G., Larson, D., Komatsu, E., et al. 2013, *ApJS*, 208, 19
- Jarvis, M., Bernstein, G., & Jain, B. 2004, *MNRAS*, 352, 338
- Kilbinger, M. & Schneider, P. 2005, *A&A*, 442, 69
- Lewis, A., Challinor, A., & Lasenby, A. 2000, *ApJ*, 538, 473
- Limber, D. N. 1953, *ApJ*, 117, 134
- Lin, C.-A. & Kilbinger, M. 2015, *A&A*, 576, A24

- Mead, A. J., Tröster, T., Heymans, C., Van Waerbeke, L., & McCarthy, I. G. 2020, *A&A*, 641, A130
- Munshi, D., McEwen, J. D., Kitching, T., et al. 2020, *J. Cosmology Astropart. Phys.*, 2020, 043
- Nishimichi, T., Takada, M., Takahashi, R., et al. 2021, *DarkEmulator: Cosmological emulation code for halo clustering statistics*
- Papoulis, A. & Pillai, S. U. 1991, *Probability, random variables, and stochastic processes*, 3rd edn. (Boston: McGraw-Hill)
- Pires, S., Leonard, A., & Starck, J.-L. 2012, *MNRAS*, 423, 983
- Planck Collaboration, Aghanim, N., Akrami, Y., et al. 2020, *A&A*, 641, A5
- Pyne, S. & Joachimi, B. 2021, *MNRAS*, 503, 2300
- Reimberg, P. & Bernardeau, F. 2018, *Phys. Rev. D*, 97, 023524
- Schneider, P. 1996, *MNRAS*, 283, 837
- Schneider, P. 1998, *ApJ*, 498, 43
- Schneider, P., Ehlers, J., & Falco, E. E. 1992, *Gravitational Lenses*, *Astronomy and Astrophysics Library* (Berlin and Heidelberg: Springer)
- Shan, H., Liu, X., Hildebrandt, H., et al. 2018, *MNRAS*, 474, 1116
- Springel, V., Yoshida, N., & White, S. D. M. 2001, *New A*, 6, 79
- Takahashi, R., Hamana, T., Shirasaki, M., et al. 2017, *ApJ*, 850, 24
- Takahashi, R., Sato, M., Nishimichi, T., Taruya, A., & Oguri, M. 2012, *ApJ*, 761, 152
- Tegmark, M., Taylor, A. N., & Heavens, A. F. 1997, *ApJ*, 480, 22
- Trotta, R. 2017, *arXiv:1701.01467*
- Uhlemann, C., Friedrich, O., Villaescusa-Navarro, F., Banerjee, A., & Codis, S. 2020, *MNRAS*, 495, 4006
- Vakili, M., Bilicki, M., Hoekstra, H., et al. 2019, *MNRAS*, 487, 3715
- Wright, A. H., Hildebrandt, H., van den Busch, J. L., et al. 2020, *A&A*, 640, L14

Appendix A: Detailed derivations for the new model

In this part of the appendix we show more detailed derivations of the results from the main text. We start with the calculation of the variances or covariances in the flat sky approximation, continue with calculations of the third order moments and finish with the derivation of the PDF of the aperture number given a smoothed density contrast by use of the characteristic function.

Appendix A.1: Variance and skewness for general filters at leading order in perturbation theory

Although analytical possible we decided against using the bi-spectrum to calculate third-order moments like the skewness. Instead we use a formalism where we calculate the second- and third-order moments of the smoothed density contrasts within cylinder of physical radius R and physical length L using the flat sky approximation shown in Appendix B in F18 for a top-hat filter, and apply it to our case with a general filter U . Numerically, this approach is faster since, as we will see below, it is possible to express the third-order moments in terms of second-order moments. Another advantage is that the projection is only along one dimension (radius of the cylinder) compared to the bi-spectrum, where the projection is at least along a 2D-grid. Following F18 we start by considering a cylinder of radius R and length L . In Fourier space the top-hat filter for such a cylinder is given by

$$W_{R,L}(\mathbf{k}) = \frac{1}{(2\pi)^3} \frac{\sin(Lk_{\parallel}/2)}{Lk_{\parallel}/2} \frac{2J_1(k_{\perp}R)}{k_{\perp}R} \equiv \frac{1}{(2\pi)^3} \frac{\sin(Lk_{\parallel}/2)}{Lk_{\parallel}/2} W_R^{\text{th}}(k_{\perp}), \quad (\text{A.1})$$

where J_1 is the first Bessel function, and k_{\parallel} and k_{\perp} are the components of \mathbf{k} parallel and orthogonal to the cylinder, respectively. The variance of the matter contrast within such a cylinder is given at leading order by

$$\langle \delta_{R,L}^2 \rangle(\chi) = D_+^2 \int dk_{\parallel} d^2k_{\perp} \frac{\sin^2(Lk_{\parallel}/2)}{(Lk_{\parallel}/2)^2} [W_R^{\text{th}}(k_{\perp})]^2 P_{\text{lin},0}(k_{\perp}) \approx \frac{2\pi D_+^2}{L} \int dk k [W_R^{\text{th}}(k)]^2 P_{\text{lin},0}(k), \quad (\text{A.2})$$

where the last expression follows from $L \gg R$, and since the integration depends from now on only on k_{\perp} we write the orthogonal component as k . The linear matter power spectrum today $P_{\text{lin},0}$ is calculated using Eisenstein & Hu (1998), and D_+ is the growth factor which depends on the conformal time. We note that the factor $1/L$ cancels out when projecting the moments in Eq. (A.28-A.30) using the Limber approximation (Limber 1953). According to this derivation for a top-hat filter we get for a general filter U that

$$W_{U_{\chi}}(k) = \int_0^{2\pi} \int_0^{\infty} dr d\vartheta U_{\chi}(r) e^{-ikr \cos \vartheta} = 2\pi \int_0^{\infty} dr J_0(kr) r U_{\chi}(r), \quad (\text{A.3})$$

where $U_{\chi}(r) = U(r/\chi) = U(\vartheta)/\chi^2$, with $U(\vartheta)$ being a filter measured in angular coordinates (see e.g. Fig. 3). Correspondingly, the variance of the matter density contrast for a general filter U in the flat sky approximation is

$$\langle \delta_{U,L}^2 \rangle(\chi) = \frac{2\pi D_+^2}{L} \int dk k W_{U_{\chi}}^2(k) P_{\text{lin},0}(k). \quad (\text{A.4})$$

Following along lines similar to those of Appendix B.4 of F18 the leading-order contribution to the skewness of matter density contrast for the general filter U can be calculated as

$$\begin{aligned} \langle \delta_{U,L}^3 \rangle(\chi) &= 3\hat{c}\pi^{-1} \int \int dq_1 dq_2 q_1 q_2 W_{U_{\chi}}(q_1) W_{U_{\chi}}(q_2) P_{\text{lin},0}(q_1) P_{\text{lin},0}(q_2) \int d\phi W_{U_{\chi}}\left(\sqrt{q_1^2 + q_2^2 + 2q_1q_2 \cos \phi}\right) F_2(q_1, q_2, \phi) \\ &\equiv 3\hat{c}\pi^{-1} \int \int dq_1 dq_2 q_1 q_2 W_{U_{\chi}}(q_1) W_{U_{\chi}}(q_2) P_{\text{lin},0}(q_1) P_{\text{lin},0}(q_2) \Phi_{U_{\chi}}(q_1, q_2), \end{aligned} \quad (\text{A.5})$$

where $\hat{c} = \frac{4\pi^2 D_+^4}{L^2}$. The function F_2 in a general Λ CDM universe is given by

$$F_2(q_1, q_2, \phi) = \frac{1}{2} \left(2 + \frac{q_1}{q_2} \cos \phi + \frac{q_2}{q_1} \cos \phi \right) + (1 + \mu) (\cos^2 \phi - 1) = 1 + \frac{1}{2} \cos \phi \left(\frac{q_1}{q_2} + \frac{q_2}{q_1} \right) - (1 - \mu) \sin^2 \phi, \quad (\text{A.6})$$

where μ results from perturbation theory and is a function of the growth factor D_+ (see Appendix B.1 in F18 or more details)⁷, and ϕ is the angle between the vectors with absolute values q_1 and q_2 . Given the definition of $W_{U_{\chi}}$ in Eq. (A.3) $\Phi_{U_{\chi}}$ can be written as

$$\Phi_{U_{\chi}}(q_1, q_2) = 2\pi \int_0^{\infty} dr r U_{\chi}(r) \int d\phi J_0\left(r \sqrt{q_1^2 + q_2^2 + 2q_1q_2 \cos \phi}\right) F_2(q_1, q_2, \phi). \quad (\text{A.7})$$

Next, we use Graf's addition theorem (see e.g. Abramowitz & Stegun 1972), which states that

$$J_0\left(\sqrt{q_1^2 + q_2^2 + 2q_1q_2 \cos \phi}\right) = \sum_{m=-\infty}^{\infty} (-1)^m J_m(q_1) J_m(q_2) e^{im\phi} = J_0(q_1) J_0(q_2) + 2 \sum_{m=1}^{\infty} (-1)^m J_m(q_1) J_m(q_2) \cos(m\phi), \quad (\text{A.8})$$

⁷ For an Einstein-de-Sitter universe $\mu = 5/7$.

such that $\Phi_{U_\chi}(q_1, q_2)$ becomes

$$\begin{aligned}
 & 2\pi \int_0^\infty r U_\chi(r) dr \int_0^{2\pi} d\phi \left[J_0(rq_1) J_0(rq_2) + 2 \sum_{m=1}^\infty (-1)^m J_m(rq_1) J_m(rq_2) \cos(m\phi) \right] \left[1 + \frac{1}{2} \cos(\phi) \left(\frac{q_1}{q_2} + \frac{q_2}{q_1} \right) - (1-\mu) \sin^2 \phi \right] \\
 &= \underbrace{2\pi^2(1+\mu) \int_0^\infty r U_\chi(r) dr J_0(rq_1) J_0(rq_2)}_A - \underbrace{2\pi^2 \int_0^\infty r U_\chi(r) dr J_1(rq_1) J_1(rq_2) \left(\frac{q_1}{q_2} + \frac{q_2}{q_1} \right)}_B + \underbrace{2\pi^2(1-\mu) \int_0^\infty r U_\chi(r) dr J_2(rq_1) J_2(rq_2)}_C,
 \end{aligned} \tag{A.9}$$

where we made use of the orthogonality of the trigonometric functions. Plugging $\Phi_{U_\chi}(q_1, q_2)$ back to Eq. (A.5) and considering each term separately we get

$$\begin{aligned}
 A : & 3\hat{c}\pi^{-1} \int \int dq_1 dq_2 q_1 q_2 W_{U_\chi}(q_1) W_{U_\chi}(q_2) P_{\text{lin},0}(q_1) P_{\text{lin},0}(q_2) 2\pi \int_0^\infty dr r U_\chi(r) \pi(1+\mu) J_0(rq_1) J_0(rq_2) \\
 &= 6\pi\hat{c}(1+\mu) \int_0^\infty dr r U_\chi(r) \left[\int dq q W_{U_\chi}(q) P_{\text{lin},0}(q) J_0(rq) \right]^2,
 \end{aligned} \tag{A.10}$$

and in analogy

$$\begin{aligned}
 C : & 3\hat{c}\pi^{-1} \int \int dq_1 dq_2 q_1 q_2 W_{U_\chi}(q_1) W_{U_\chi}(q_2) P_{\text{lin},0}(q_1) P_{\text{lin},0}(q_2) 2\pi \int_0^\infty dr r U_\chi(r) \pi(1-\mu) J_2(rq_1) J_2(rq_2) \\
 &= 6\pi\hat{c}(1-\mu) \int_0^\infty dr r U_\chi(r) \left[\int dq q W_{U_\chi}(q) P_{\text{lin},0}(q) J_2(rq) \right]^2,
 \end{aligned} \tag{A.11}$$

and finally

$$\begin{aligned}
 B : & -3\hat{c}\pi^{-1} \int \int dq_1 dq_2 q_1 q_2 W_{U_\chi}(q_1) W_{U_\chi}(q_2) P_{\text{lin},0}(q_1) P_{\text{lin},0}(q_2) 2\pi \int_0^\infty dr r U_\chi(r) \pi J_1(rq_1) J_1(rq_2) \left[\frac{q_1}{q_2} + \frac{q_2}{q_1} \right] \\
 &= -12\pi\hat{c} \int_0^\infty dr r U_\chi(r) \int dq_1 q_1^2 W_{U_\chi}(q_1) P_{\text{lin},0}(q_1) J_1(rq_1) \int dq_2 W_{U_\chi}(q_2) P_{\text{lin},0}(q_2) J_1(rq_2).
 \end{aligned} \tag{A.12}$$

The following transformations are just in order to have a more compressed expression for $\langle \delta_{U_\chi, L}^3 \rangle(\chi)$, which can then be used to verify our derivation by comparing it with the result from F18 for a top-hat filter. For this, we rewrite the expression of Bessel functions in terms of $W_r^{\text{th}}(q)$ as

$$J_2(rq) = \frac{1}{rq} J_1(rq) - \frac{1}{q} \frac{d}{dr} J_1(rq) = \frac{1}{rq} J_1(rq) - \left[r \frac{d}{dr} \frac{J_1(rq)}{rq} + \frac{1}{rq} J_1(rq) \right] = -\frac{1}{2} \frac{d}{d \ln(r)} W_r^{\text{th}}(q), \tag{A.13}$$

$$J_0(rq) = \frac{1}{rq} J_1(rq) + \frac{1}{q} \frac{d}{dr} J_1(rq) = \frac{1}{rq} J_1(rq) + \left[r \frac{d}{dr} \frac{J_1(rq)}{rq} + \frac{1}{rq} J_1(rq) \right] = W_r^{\text{th}}(q) + \frac{1}{2} \frac{d}{d \ln(r)} W_r^{\text{th}}(q), \tag{A.14}$$

and with

$$\frac{1}{rq} \frac{d^2}{dr^2} J_1(rq) = \frac{1}{2} \frac{d^2}{dr^2} W_r^{\text{th}}(q) - \frac{2}{r^2} \left[\frac{1}{rq} J_1(rq) - \frac{1}{q} \frac{d}{dr} J_1(rq) \right] = \frac{1}{2} \frac{d^2}{dr^2} W_r^{\text{th}}(q) + \frac{1}{r^2} \frac{d}{d \ln(r)} W_r^{\text{th}}(q), \tag{A.15}$$

we get

$$rq J_1(rq) = J_2(rq) - rq \frac{1}{q^2} \frac{d^2}{dr^2} J_1(rq) = J_2(rq) - r^2 \frac{1}{rq} \frac{d^2}{dr^2} J_1(rq) = -\frac{3}{2} \frac{d}{d \ln(r)} W_r^{\text{th}}(q) - \frac{r^2}{2} \frac{d^2}{dr^2} W_r^{\text{th}}(q). \tag{A.16}$$

These relation together with the following notation

$$Q_1(r, \chi) = \frac{2\pi D_+^2}{L} \int dk k W_{U_\chi}(k) W_r^{\text{th}}(k) P_{\text{lin},0}(k), \tag{A.17}$$

$$Q_2(r, \chi) = \frac{2\pi D_+^2}{L} \int dk k W_{U_\chi}(k) \frac{d}{d \ln(r)} W_r^{\text{th}}(k) P_{\text{lin},0}(k), \tag{A.18}$$

$$Q_3(r, \chi) = \frac{2\pi D_+^2}{L} \int dk k W_{U_\chi}(k) \frac{d^2}{dr^2} W_r^{\text{th}}(k) P_{\text{lin},0}(k). \tag{A.19}$$

we find that

$$A : \quad 6\pi\hat{c}(1+\mu) \int_0^\infty dr r U_\chi(r) \left[\int dq q W_{U_\chi}(q) P_{\text{lin},0}(q) J_0(rq) \right]^2 = 6\pi(1+\mu) \int_0^\infty dr r U_\chi(r) \left[Q_1(r, \chi) + \frac{1}{2} Q_2(r, \chi) \right]^2, \quad (\text{A.20})$$

$$C : \quad 6\pi\hat{c}(1-\mu) \int_0^\infty dr r U_\chi(r) \left[\int dq q W_{U_\chi}(q) P_{\text{lin},0}(q) J_2(rq) \right]^2 = 6\pi(1-\mu) \int_0^\infty dr r U_\chi(r) \left[-\frac{1}{2} Q_2(r, \chi) \right]^2, \quad (\text{A.21})$$

and

$$\begin{aligned} B : \quad & -12\pi\hat{c} \int_0^\infty dr r U_\chi(r) \int dq_1 q_1 W_{U_\chi}(q_1) P_{\text{lin},0}(q_1) r q_1 J_1(rq_1) \int dq_2 q_2 W_{U_\chi}(q_2) P_{\text{lin},0}(q_2) \frac{1}{r q_2} J_1(rq_2) \\ & = -12\pi \int_0^\infty dr r U_\chi(r) \left[-\frac{3}{2} Q_2(r, \chi) - \frac{r^2}{2} Q_3(r, \chi) \right] \frac{1}{2} Q_1(r, \chi). \end{aligned} \quad (\text{A.22})$$

Finally combining A, B and C the skewness of $\delta_{U_\chi, L}$ simplifies to

$$\begin{aligned} \langle \delta_{U_\chi, L}^3 \rangle(\chi) &= 6\pi \int_0^\infty dr r U_\chi(r) \left((1+\mu) \left[Q_1(r, \chi) + \frac{1}{2} Q_2(r, \chi) \right]^2 + (1-\mu) \frac{1}{4} Q_2^2(r, \chi) + \frac{3}{2} Q_1(r, \chi) Q_2(r, \chi) + \frac{r^2}{2} Q_1(r, \chi) Q_3(r, \chi) \right) \\ &= 3\pi \int_0^\infty dr r U_\chi(r) \left(2(1+\mu) \left[Q_1^2(r, \chi) + Q_1(r, \chi) Q_2(r, \chi) \right] + 3Q_1(r, \chi) Q_2(r, \chi) + Q_2^2(r, \chi) + r^2 Q_1(r, \chi) Q_3(r, \chi) \right) \\ &= 3\pi \int_0^\infty dr U_\chi(r) \frac{d}{dr} \left(r^2 \left[(1+\mu) Q_1^2(r, \chi) + Q_1(r, \chi) Q_2(r, \chi) \right] \right), \end{aligned} \quad (\text{A.23})$$

where it is seen that for a top-hat of size ϑ with $U_\chi(r) = \mathcal{H}(\vartheta - \chi r)$ the result in Eq. (B.35) immediately follows.

Although all necessary ingredients for specifying the PDF of $\delta_{m, U}$ are derived already, we still need moments like $\langle \delta_{\chi\vartheta, L} \delta_{U, L}^2 \rangle(\chi)$ to compute quantities like $\langle \kappa_{<\vartheta} | \delta_{m, U} \rangle$ or $\langle w_{<\vartheta} \delta_{m, U}^k \rangle$. With the definitions of two further integrals,

$$Q_4(r, \chi\vartheta) = \frac{2\pi D_+^2}{L} \int dq q W_{\chi\vartheta}^{\text{th}}(q) P_{\text{lin}}(q) W_r^{\text{th}}(q), \quad (\text{A.24})$$

$$Q_5(r, \chi\vartheta) = \frac{2\pi D_+^2}{L} \int dq q W_{\chi\vartheta}^{\text{th}}(q) P_{\text{lin}}(q) \frac{d}{d \ln r} W_r^{\text{th}}(q), \quad (\text{A.25})$$

and using the result of F18 that for a top-hat filter of size R

$$\Phi_R^{\text{th}}(q_1, q_2) = \int d\phi W_R^{\text{th}} \left(\sqrt{q_1^2 + q_2^2 + 2q_1 q_2 \cos \phi} \right) F_2(q_1, q_2, \phi) = \pi(1+\mu) W_R^{\text{th}}(q_1) W_R^{\text{th}}(q_2) + \frac{\pi}{2} \frac{d}{d \ln R} \left[W_R^{\text{th}}(q_1) W_R^{\text{th}}(q_2) \right], \quad (\text{A.26})$$

the joint filter moments between the matter density contrast smoothed with the general filter and the matter density contrast smoothed with a top-hat of size ϑ follows in analogy to the skewness, and is given by

$$\begin{aligned} \langle \delta_{\vartheta, L} \delta_{U, L}^2 \rangle(\chi) &= \frac{\hat{c}}{\pi} \int \int dq_1 dq_2 q_1 q_2 W_{U_\chi}(q_1) W_{U_\chi}(q_2) P_{\text{lin},0}(q_1) P_{\text{lin},0}(q_2) \Phi_{\chi\vartheta}^{\text{th}}(q_1, q_2) + \\ &\quad \frac{2\hat{c}}{\pi} \int \int dq_1 dq_2 q_1 q_2 W_{U_\chi}(q_1) W_{\chi\vartheta}^{\text{th}}(q_2) P_{\text{lin},0}(q_1) P_{\text{lin},0}(q_2) \Phi_{U_\chi}(q_1, q_2) \\ &= (1+\mu) Q_1^2(\chi\vartheta, \chi) + Q_1(\chi\vartheta, \chi) Q_2(\chi\vartheta, \chi) + \\ &\quad 2\pi \int dr U_\chi(r) \frac{d}{dr} \left(r^2 (1+\mu) Q_1(r, \chi) Q_4(r, \chi\vartheta) + \frac{r^2}{2} [Q_1(r, \chi) Q_5(r, \chi\vartheta) + Q_2(r, \chi) Q_4(r, \chi\vartheta)] \right). \end{aligned} \quad (\text{A.27})$$

Appendix A.2: Limber projection

Given the moments of the smoothed density contrasts at comoving distance χ derived in the foregoing section, the moments in Eqs. (24, 25) and Eqs. (31–33) for $k = 1, 2$ or 3 follow (see e.g. Bernardeau & Valageas 2000),

$$\langle \delta_{m,U}^k \rangle = \int d\chi q_f^k(\chi) L^{k-1} \langle \delta_{U,L}^k \rangle(\chi), \quad (\text{A.28})$$

$$\langle \kappa_{<\vartheta} \delta_{m,U}^k \rangle = \int d\chi W_s(\chi) q_f^k(\chi) L^{k-1} \langle \delta_{\vartheta,L} \delta_{U,L}^k \rangle(\chi), \quad (\text{A.29})$$

$$\langle w_{<\vartheta} \delta_{m,U}^k \rangle = \int d\chi q_f^{k+1}(\chi) L^{k-1} \langle \delta_{\vartheta,L} \delta_{U,L}^k \rangle(\chi), \quad (\text{A.30})$$

where $q_f(\chi)$ is the projection kernel defined in Eq. (10) and $W_s(\chi)$ the lensing efficiency defined in Eq. (14). We note that these three foregoing equations employ a Limber approximation which consist of $L \rightarrow \infty$ (Limber 1953), and that the physical radius r of filter U scales with χ as described below Eq. (A.3). We also note that the foregoing expectation values are independent of L .

Appendix A.3: Non-linear regime

In order to go to the non-linear regime for second-order moments we replace the linear power spectrum in the above calculations with the non-linear power spectrum, which in turn is determined with the halo fit model from Takahashi et al. (2012) using an analytic approximation for the transfer function (Eisenstein & Hu 1998).

For the third-order moments we use that for a top-hat filter of size R the filter simplifies to $U_\chi(r) = \frac{1}{\pi R^2} \mathcal{H}(R - r)$, such that

$$\begin{aligned} Q_1(R, \chi) &= \frac{2\pi D_+^2}{L} \int dk k W_{U_\chi}(k) W_R^{\text{th}}(k) P_{\text{lin},0}(k) \\ &= \frac{2\pi D_+^2}{L} \int dk k W_R^{\text{th}}(k) W_R^{\text{th}}(k) P_{\text{lin},0}(k) \\ &= \langle \delta_{R,L}^2 \rangle(\chi), \end{aligned} \quad (\text{A.31})$$

and

$$\begin{aligned} Q_2(R, \chi) &= \frac{2\pi D_+^2}{L} \int dk k W_{U_\chi}(k) \frac{d}{d \ln(r)} W_R^{\text{th}}(k) P_{\text{lin},0}(k) \\ &= \frac{2\pi D_+^2}{L} \int dk k W_R^{\text{th}}(k) \frac{d}{d \ln(R)} W_R^{\text{th}}(k) P_{\text{lin},0}(k) \\ &= \frac{1}{2} \frac{d}{d \ln(R)} \langle \delta_{R,L}^2 \rangle(\chi). \end{aligned} \quad (\text{A.32})$$

Furthermore, the skewness simplifies in this case to:

$$\langle \delta_{R,L}^3 \rangle(\chi) = 3(1 + \mu) \langle \delta_{R,L}^2 \rangle^2(\chi) + \frac{3}{2} \langle \delta_{R,L}^2 \rangle(\chi) \frac{d \langle \delta_{R,L}^2 \rangle(\chi)}{d \ln(R)}. \quad (\text{A.33})$$

This then helps to define

$$S_3 \equiv \frac{\langle \delta_{R,L}^3 \rangle(\chi)}{\langle \delta_{R,L}^2 \rangle^2(\chi)} = 3(1 + \mu) + \frac{3}{2} \frac{d}{d \ln(R)} \ln \langle \delta_{R,L}^2 \rangle, \quad (\text{A.34})$$

which is in the linear and in the non-linear regime approximately the same (Bernardeau et al. 2002), meaning that in order to get the skewness in the non-linear regime we approximate

$$\langle \delta_{R,L}^3 \rangle_{\text{non-linear}}(\chi) \approx S_3 \langle \delta_{R,L}^2 \rangle_{\text{non-linear}}^2(\chi). \quad (\text{A.35})$$

For the general filter we use that the numerical integration of r in $\langle \delta_{U_\chi,L}^3 \rangle(\chi)$ results basically into a sum of top-hat filters, such that we make use of S_3 to scale each term individual to the non-linear regime. For the joint filter moment $\langle \delta_{\chi\vartheta,L} \delta_{U_\chi,L}^2 \rangle(\chi)$ we use of generalised version of S_3 , which states that for two different top-hat filter of size R_1 and R_2

$$\langle \delta_{R_1,L}^2 \delta_{R_2,L} \rangle(\chi) \propto \langle \delta_{R_1,L} \delta_{R_2,L} \rangle(\chi) \langle \delta_{R_1,L}^2 \rangle(\chi). \quad (\text{A.36})$$

Using again that the r -integration results into a sum of top-hat filter and factor out the non-derivative terms similar to Eq. (A.34), we scale individual all those non-derivative terms to the non-linear regime.

Appendix A.4: Characteristic function

We consider a large circle of radius R , inside of which there are $N = n_0 \pi R^2$ galaxies, where n_0 is the galaxy number density. The probability of finding a galaxy at separation ϑ is

$$p(\vartheta; \delta_{m,U}) = \frac{2\vartheta}{R^2 \eta} (1 + b \langle w_\vartheta | \delta_{m,U} \rangle), \quad (\text{A.37})$$

where $\langle w_\vartheta | \delta_{m,U} \rangle$ is the expectation of the mean 2D density contrast on a circle at ϑ (see Eq. 37) given the smoothed density contrast defined in Eq. (38). The assumption of linear galaxy bias enters here by the term $b \langle w_\vartheta | \delta_{m,U} \rangle$. The normalisation is

$$\eta = \int_0^R \frac{2\vartheta}{R^2} (1 + b \langle w_\vartheta | \delta_{m,U} \rangle) d\vartheta, \quad (\text{A.38})$$

which goes to unity for $R \rightarrow \infty$. The characteristic function (CF) of the aperture number N_{ap} , given the smoothed 2D density contrast $\delta_{m,U}$, is given by

$$\begin{aligned} \Psi(t) &= \langle e^{itN_{\text{ap}}} \rangle_{\delta_{m,U}} = \int_{\mathbb{R}} dN_{\text{ap}} p(N_{\text{ap}} | \delta_{m,U}) e^{itN_{\text{ap}}} \\ &= \left[\prod_{i=1}^N \int_0^R d\vartheta_i p(\vartheta_i; \delta_{m,U}) \right] e^{it \sum_j U(\vartheta_j)} \\ &= \left[\int_0^R d\vartheta \frac{2\vartheta}{R^2 \eta} (1 + b \langle w_\vartheta | \delta_{m,U} \rangle) e^{itU(\vartheta)} \right]^N \\ &= \left[\int_0^R d\vartheta \frac{2\vartheta}{R^2 \eta} (1 + b \langle w_\vartheta | \delta_{m,U} \rangle) (e^{itU(\vartheta)} - 1 + 1) \right]^N \\ &= \left[1 + \frac{\pi n_0}{N \eta} \int_0^R d\vartheta 2\vartheta (1 + b \langle w_\vartheta | \delta_{m,U} \rangle) (e^{itU(\vartheta)} - 1) \right]^N \\ &\xrightarrow[N, R \rightarrow \infty]{} \exp \left[2\pi n_0 \int_0^\infty d\vartheta \vartheta (1 + b \langle w_\vartheta | \delta_{m,U} \rangle) (e^{itU(\vartheta)} - 1) \right], \end{aligned}$$

where we used in the second line that

$$N_{\text{ap}} = \int_0^\infty d^2\vartheta U(|\vartheta|) n(\vartheta) = \sum_j U(\vartheta_j),$$

with $n(\vartheta) = \sum_j \delta_D(\vartheta - \vartheta_j)$, and that the galaxy positions ϑ_i independently trace the density profile $\langle w_\vartheta | \delta_{m,U} \rangle$. As discussed in Sect. 3.3 the exact approach is to transform the CF to the probability density function $p(N_{\text{ap}} | \delta_{m,U})$ by use of the inverse Fourier transformation. Alternatively, we assume that the PDF is well approximated by a log-normal distribution as

$$p(N_{\text{ap}} | \delta_{m,U}) = \frac{1}{\sqrt{2\pi} S (N_{\text{ap}} + L)} \exp \left(- \frac{[\ln(N_{\text{ap}} + L) - M]^2}{2S^2} \right),$$

(A.39)

where the parameters S, M, L are fixed with the first raw moment

$$\mu'_1 = \langle N_{\text{ap}} | \delta_{\text{m},U} \rangle = \langle N_{\text{ap}} \rangle_{\delta_{\text{m},U}} = \exp\left(M + \frac{S^2}{2}\right) - L, \quad (\text{A.40})$$

and the central moments

$$\mu_2 = \langle (N_{\text{ap}} - \langle N_{\text{ap}} \rangle)^2 \rangle_{\delta_{\text{m},U}} = \exp(2M + S^2) [e^{S^2} - 1], \quad (\text{A.41})$$

$$\mu_3 = \langle (N_{\text{ap}} - \langle N_{\text{ap}} \rangle)^3 \rangle_{\delta_{\text{m},U}} = \exp\left(3M + \frac{3}{2}S^2\right) [e^{S^2} - 1]^2 [e^{S^2} + 2]. \quad (\text{A.42})$$

The raw moments can be calculated from the derivatives of the CF,

$$\mu'_n = \frac{d^n \Psi(t)}{d(it)^n} \Big|_{t=0}. \quad (\text{A.43})$$

With the definition

$$E_n = 2\pi n_0 \int_0^\infty d\vartheta \vartheta (1 + b \langle w_\vartheta | \delta_{\text{m},U} \rangle) U^n(\vartheta), \quad (\text{A.44})$$

it follows that

$$\begin{aligned} \mu'_0 &= 1, \\ \mu'_1 &= E_1, \\ \mu'_2 &= (E_1)^2 + E_2, \\ \mu'_3 &= (E_1)^3 + 3E_1E_2 + E_3, \end{aligned} \quad (\text{A.45})$$

and so

$$\mu_2 = \mu'_2 - (\mu'_1)^2 = (E_1)^2 + E_2 - (E_1)^2 = E_2, \quad (\text{A.46})$$

$$\mu_3 = \mu'_3 - 3\mu'_1\mu'_2 + 2(\mu'_1)^3 = E_3. \quad (\text{A.47})$$

To find the parameters of the log-normal distribution Eq. (A.39) by use of the raw and central moments in Eqs. (A.45–A.47) we define

$$\begin{aligned} \gamma &= \frac{\mu_3}{\mu_2^{3/2}} = \sqrt{\exp(S^2) - 1} [2 + \exp(S^2)] \\ &= \sqrt{q - 1} (2 + q), \end{aligned} \quad (\text{A.48})$$

where we defined in the last step $q = \exp(S^2)$. Modifying γ we get

$$0 = q^3 + 3q^2 - 4 - \gamma^2, \quad (\text{A.49})$$

which always has one real solution q_0 , and so the parameters follow to

$$S = \sqrt{\ln(q_0)}, \quad (\text{A.50})$$

$$M = \frac{1}{2} \ln\left(\frac{\mu_2}{q_0^2 - q_0}\right), \quad (\text{A.51})$$

$$L = \sqrt{\frac{\mu_2}{q_0 - 1}} - \mu'_1. \quad (\text{A.52})$$

To check this derivation and compare it to the direct approach of using the inverse Fourier transformation, we created an idealised case of a full-sky uniform random field $n_{\text{side}} = 4096$ with a number density $n_0 \approx 0.034/\text{arcmin}^2$. Next we calculated by use of the HEALPY internal SMOOTHING function N_{ap} for the top-hat filter

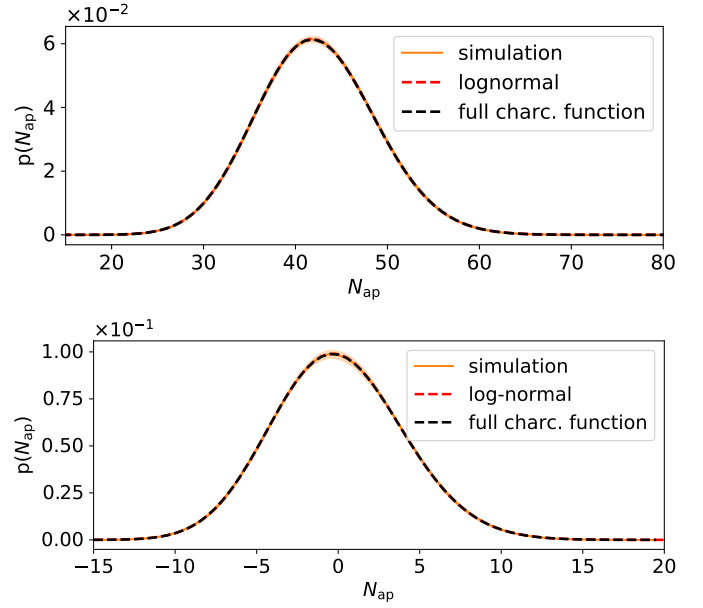


Fig. A.1: Probability distribution of the aperture number resulting a uniform random field smoothed with the top-hat filter of size $20'$ in the upper panel and for the adapted filter U of size $120'$ in the lower panel. The orange shaded region is the standard deviation determined from 48 sub-patches.

of size $20'$ and the for the adapted filter. In the determination of the predicted PDF we set $\langle w_\vartheta | \delta_{\text{m},U} \rangle = 0$ so $p(N_{\text{ap}})$ follows immediately with Eq. (A.39) or Eq. (42). It is clearly seen in Fig. A.1 that model for both filters fits excellent with the measured PDF of the aperture number. Additionally we show in Fig. A.2 a comparison between the predicted $p(N_{\text{ap}})$ using the full characteristic function Eq. (36) versus the log-normal approach Eq. (A.39) for the low-redshift bin z_l^{low} from the Takahashi setup. In the lower panel the residual difference between both methods is three orders of magnitude smaller than the signal itself, which shows that both approaches are identically given the uncertainties we expect for Stage-III surveys. Since the log-normal approach is faster to compute we can use this approach in future analysis, where computational speed is essential.

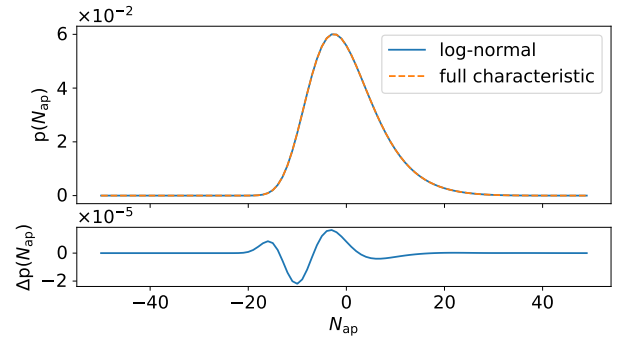


Fig. A.2: Comparison between the two approaches to calculate $p(N_{\text{ap}})$. It is clearly seen that both methods yield almost the same result.

Appendix B: Corrections formulae for the power spectra of the T17 simulations

To account for the finite angular resolution T17 suggested a simple damping factor at small scales as

$$C_\ell^\kappa \rightarrow \frac{C_\ell^\kappa}{1 + (\ell/\ell_{\text{res}})^2}, \quad (\text{B.1})$$

where $\ell_{\text{res}} = 1.6 \times N_{\text{side}}$. Additionally to take the shell thickness into account they conducted a simple fitting formula by which the matter power spectrum should be modified to

$$P_\delta(k) \rightarrow P_\delta^W(k) = \frac{(1 + c_1 k^{-\alpha_1})^{\alpha_1}}{(1 + c_2 k^{-\alpha_2})^{\alpha_3}} P_\delta(k), \quad (\text{B.2})$$

where the parameters are simulation specific and are $c_1 = 9.5171 \times 10^{-4}$, $c_2 = 5.1543 \times 10^{-3}$, $\alpha_1 = 1.3063$, $\alpha_2 = 1.1475$, $\alpha_3 = 0.62793$, and the wavenumber k is in units of h/Mpc . We note that although we incorporated these corrections in the following, they have only a very little effect on the scales we are considering.

Appendix C: Complementary material

Table C.1: Overview of all the different cosmological parameters for the 26 cosmo-SLICS models, which are used in Sect. 5 for the cosmological analysis.

	Ω_m	h	w_0	σ_8	S_8
fid	0.2905	0.6898	-1.0000	0.8364	0.8231
1	0.3282	0.6766	-1.2376	0.6677	0.6984
2	0.1019	0.7104	-1.6154	1.3428	0.7826
3	0.2536	0.6238	-1.7698	0.6670	0.6133
4	0.1734	0.6584	-0.5223	0.9581	0.7284
5	0.3759	0.6034	-0.9741	0.8028	0.8986
6	0.4758	0.7459	-1.3046	0.6049	0.7618
7	0.1458	0.8031	-1.4498	1.1017	0.7680
8	0.3099	0.6940	-1.8784	0.7734	0.7861
9	0.4815	0.6374	-0.7737	0.5371	0.6804
10	0.3425	0.8006	-1.5010	0.6602	0.7054
11	0.5482	0.7645	-1.9127	0.4716	0.6375
12	0.2898	0.6505	-0.6649	0.7344	0.7218
13	0.4247	0.6819	-1.1986	0.6313	0.7511
14	0.3979	0.7833	-1.1088	0.7360	0.8476
15	0.1691	0.7890	-1.6903	1.1479	0.8618
16	0.1255	0.7567	-0.9878	0.9479	0.6131
17	0.5148	0.6691	-1.3812	0.6243	0.8178
18	0.1928	0.6285	-0.8564	1.1055	0.8862
19	0.2784	0.7151	-1.0673	0.6747	0.6500
20	0.2106	0.7388	-0.5667	1.0454	0.8759
21	0.4430	0.6161	-1.7037	0.6876	0.8356
22	0.4062	0.8129	-1.9866	0.5689	0.6620
23	0.2294	0.7706	-0.8602	0.9407	0.8226
24	0.5095	0.6988	-0.7164	0.5652	0.7366
25	0.3652	0.7271	-1.5414	0.5958	0.6574

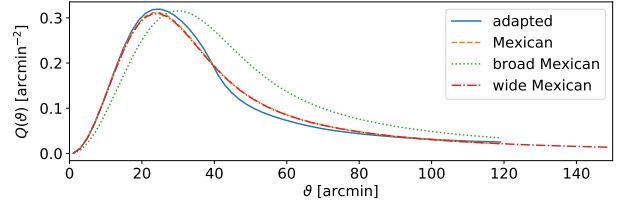


Fig. C.1: Different filters Q resulting from the corresponding U filters show in Fig. 3 used in this work to verify the new model.